

Subsistence of ice-covered lakes during the Hesperian at Gale crater, Mars

Alexandre M. Kling^{a,b}, Robert M. Haberle^b, Christopher P. McKay^c, Thomas F. Bristow^d,
Frances Rivera-Hernandez^e

^aBay Area Environmental Research Institute, Moffett Field, CA 94035

^bPlanetary Systems Branch, NASA Ames Research Center, Moffett Field, CA 94035

^cSpace Science and Astrobiology Division, NASA Ames Research Center, Moffett Field, CA 94035, USA

^dExobiology Branch, NASA Ames Research Center, Moffett Field, CA 94035

^eDartmouth College, Davis, Hanover, NH 03755

Abstract

Sedimentary deposits characterized by the Mars Science Laboratory *Curiosity* rover provide evidence that Gale crater, Mars intermittently hosted a fluvio-lacustrine environment during the Hesperian. However, estimates of the CO₂ content of the atmosphere at the time the sediments in Gale crater were deposited are far less than needed by any climate model to maintain temperatures warm enough for sustained open water lake conditions due to the low solar energy input available at that time. To reconcile some of the in-situ sedimentological evidence for liquid water with climate modeling studies, we perform the water budget of evaporation against precipitation to estimate the minimum lifetimes and the rainfall requirements for open water and ice-covered lakes in Gale crater, for a wide range of pressures and temperatures. We found that both open water and ice-covered lakes are possible, and that ice-covered lakes provide better consistency in regards of the low erosion rates estimates for the Hesperian. We incrementally test the existence of open water conditions using energy balance calculations for the global, regional, and seasonal temperatures, and we assess if the preservation of liquid water was possible under perennial ice covers. We found scenarios where lacustrine conditions are preserved in a cold climate, where the resupply of water by the inflow of rivers and high precipitation rates are substituted by an abutting glacier. For equatorial temperatures as low as 240K-255K, the ice thickness ranges from 3-10 m, a value comparable to the range of those for the perennially ice-covered lakes in Antarctica (3-6 m). The ice-covered lake hypothesis is a compelling way to decouple the mineralogy and the climate by limiting the gas exchanges between the sediment and the CO₂ atmosphere, and it eliminates the requirement for global mean temperatures above the freezing point. Not only do ice-covered lakes provide a baseline for exploring the range of possible lake scenarios for Gale crater during the Hesperian that is fully consistent with climate studies, but also they might have been ideal environments to sustain life on Mars.

Contents

1	Introduction	2
2	Water budget: precipitation requirements for open water and frozen lakes	2
3	Temperature requirements for open water lakes	6
4	The ice-covered lakes hypothesis	13
5	Summary and caveats for the ice-covered lake hypothesis	19
6	Appendix	20

removal of the saturated water vapor from the air/water interface: free convection, which is driven by the buoyancy of water vapor into the denser CO₂ atmosphere, and forced convection which is a result of the winds advecting the water vapor away from the source.

On Earth, boundary layers above non-heated lakes are nearly neutrally stable, thus the evaporation is dominated by forced convection (Adams et al., 1990). On the other hand, on Mars, due to the low atmospheric pressure, free convection is significant and temperature-dependent. Chittenden et al. (2008) found experimentally that at low relative humidity ($\approx 1\%$) and at a temperature of -15°C , the evaporation rate is $E = 0.68 + 0.025V[\text{mm.hr}^{-1}]$ with V the wind speed in m.s^{-1} . However, they observed almost no dependence of the evaporation rate on the wind speed in high relative humidity atmospheres ($RH = 30\text{-}35\%$).

On early Mars, the situation could have been in between these two cases. A potential caveat is that as the wind speed increases, turbulent mixing homogenizes the CO₂/water vapor mixture above the lake which tends to shut down the transport by buoyancy of the saturated air at the very surface of the lake toward the 'conceptually dry' ambient air. To mitigate an over-estimation of the evaporation rate, we use the norm of the free and forced evaporative fluxes in place of their linear sum, so the total evaporation quickly converges toward either the purely free or the purely convective asymptotes in the case where one process dominates the other (Adams et al., 1990).

We first consider that the lakes during the Hesperian were either open water or ice-covered and following Ingersoll (1971), Adams et al. (1990) and Dundas and Byrne (2010) we compute the sublimation and evaporation rates combining free and forced convection:

$$E_{combined} = \frac{1}{\rho_{H_2O}} \left(\underbrace{(K_M)^2}_{free} + \underbrace{(A u)^2}_{forced} \right)^{\frac{1}{2}} \times \underbrace{\frac{M_{H_2O}}{R} \left(\frac{e_{sat}^{surf}}{T_{surf}} - RH \frac{e_{sat}^{atm}}{T_{atm}} \right)}_{T \text{ and } RH \text{ dependent}} \quad [\text{m/s}] \quad (1)$$

with ρ_{H_2O} the density of either water or ice which is used to convert the evaporation rate from $\text{kg.m}^{-2}\text{s}^{-1}$ to m.s^{-1} , K_M a bulk coefficient for the diffusion of water vapor into the denser CO₂ atmosphere in unit of m s^{-1} , A a function characterizing the magnitude of the wind-driven convection, u the wind speed, M_{H_2O} the molar mass of the water, R the gas constant, RH the relative humidity, T_{surf} and T_{atm} respectively the lake's surface temperature and the atmospheric temperature (with $T_{surf} \geq T_{atm}$), e_{sat}^{surf} and e_{sat}^{atm} the saturated partial pressure of H₂O evaluated respectively at T_{surf} and T_{atm} over water or ice. The expressions used for K_M and A are given in the Appendix.

To assess which combinations of pressure and temperature could have been compatible with long lived lakes ($>10,000$ years e.g. Grotzinger et al. (2015)), we derive two metrics from the evaporation rate: a) the minimum lake lifetime and b) the precipitation rate required to sustain the constant water levels. Plausible values for the humidity, surface wind speed, geometry of the lake and water run-off are proposed in Table 1 and the derivation of the parameters from Eq. (1) is detailed in the Appendix.

Minimum lake lifetime and precipitation rates

First, the minimum lifetime of a lake is obtained assuming no resupply of the lake through rainfall, ground water flow, or run-off. In other words the lifetime of a lake simply corresponds to the time required to evaporate the water column at the deepest point of the lake:

$$\tau_{lake} = \frac{h_{lake}}{E_{combined}} \quad [\text{yr}] \quad (2)$$

with h_{lake} the maximum depth of the lake, $E_{combined}$ the evaporation rate from Eq. (1) in unit of Earth years.

In order to compute the precipitation rate, we need to know the total catchment area. We approximate Gale crater as a parabolic crater of diameter $2R_{Gale}=150$ km, maximum depth $h_{Gale} = 3\text{km}$ and without a central mound (the presence of a mound has no impact on the catchment area calculation). This geometry provides a reasonable fit of the present-day crater's topography, including the North/South asymmetry. The lake is represented as a spherical cap to relate the radius of the lake to its maximum depth (see Figure 2):

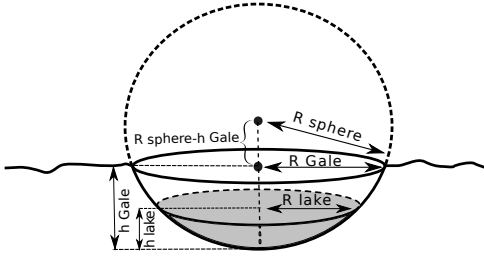


Figure 2: The spherical cap approximation for a lake (in grey) sitting at the bottom of a parabolic crater relates the depth of the lake to its catchment area

Parameter	Value	Justification
Relative humidity	50%	humid climate, comparable to the annual mean value on the American Pacific Coast. (NOAA, 2015)
Surface winds	5 m/s	arbitrary value, typical for Mars based on climate modeling
Run-off coefficient	20%	typical for sandy soils with of <7% slope (AASCE, 1993)
Depth of the lake	~100m	based on 75 m stratigraphy traversed by MSL (Grotzinger et al., 2015)

Table 1: Assumptions for our model

$$\begin{cases}
 (R_{sphere} - h_{Gale})^2 + R_{Gale}^2 = R_{sphere}^2 \\
 (R_{sphere} - h_{lake})^2 + R_{lake}^2 = R_{sphere}^2
 \end{cases}
 \quad (3)$$

$$\Rightarrow \begin{cases}
 R_{sphere} = \frac{R_{lake}^2 + h_{lake}^2}{2h_{lake}} \\
 R_{lake} = \sqrt{2R_{sphere} h_{lake} - h_{lake}^2}
 \end{cases}$$

A 100m deep lake sitting in a 150km diameter/3 km deep parabolic crater has a diameter of approximately 27km, resulting in a catchment area $S_{catch} = \pi(R_{Gale}^2 - R_{lake}^2) \approx 17000 \text{ km}^2$ about 29 times bigger than the lake's area itself. The contribution of the catchment areas up-slope of Peace Vallis (730 km^2), Dulce Vallis (450 km^2) (Palucis et al., 2014), and other minor fans extending beyond the crater's rims make altogether less than 7 % of the crater's catchment area and are neglected in this calculation.

The precipitation rates required to sustain the water level must exactly compensate the evaporation rates in a closed basin (i.e. no ground water recharge) (Matsubara et al., 2011):

$$(S_{lake} + \alpha_R S_{catch})P - S_{lake}E = 0 \quad (4)$$

with S_{lake} the lake area, α_R the run-off coefficient which represents the fraction of the water deposited on the catchment area that enters the lake, S_{catch} the catchment area, P the precipitation rate and E the evaporation rate. We assume that the precipitation that does not run-off either evaporates on the slopes or infiltrates a water table that is not connected to the lake system. The precipitation rate therefore represents a maximum rate since groundwater could have also fed the lake.

Reorganizing Eq. (4), we have for the precipitation:

$$P = \frac{E}{1 + \alpha_R \left(\frac{R_{Gale}^2}{R_{lake}^2} - 1 \right)} \approx \frac{E}{1 + 29 \alpha_R} \quad [m/s] \quad (5)$$

Implications for the Hesperian climate

Using Eq. (1) and assuming $T_{surf} \approx T_{atm} = \overline{T}_R$, with \overline{T}_R the annually-averaged regional temperature near Gale's latitude, we compute the evaporation rate, the minimum lifetime of a lake, and the precipitation rate required to sustain the water level, as a function of pressure and temperature 3.6 Gya. The results are shown in Figure 3 for 5 m/s surface winds, a run-off coefficient of 20%, and a constant relative humidity of 50%. Such a value for the humidity is, by definition, rather high for hyper-arid climates and therefore provides conservative (low) evaporation rates for the cold cases ($\overline{T}_R < 273\text{K}$). Similarly, Table 2 shows the precipitation rates for a reference

2 WATER BUDGET: PRECIPITATION REQUIREMENTS FOR OPEN WATER AND FROZEN LAKES

Wind speed	1 m/s	5 m/s	10 m/s
Evap. rate	34 cm/yr	167 cm/yr	334 cm/yr
Prec. rate, $\alpha_R=0\%$	35 cm/yr	167 cm/yr	334 cm/yr
Prec. rate, $\alpha_R=20\%$	5 cm/yr	24 cm/yr	49 cm/yr
Prec. rate, $\alpha_R=100\%$	1 cm/yr	6 cm/yr	11 cm/yr

Table 2: Evaporation and precipitation rates as a function of the run-off coefficient and the surface wind speed. T=273K, P=500 mbar, RH=50%

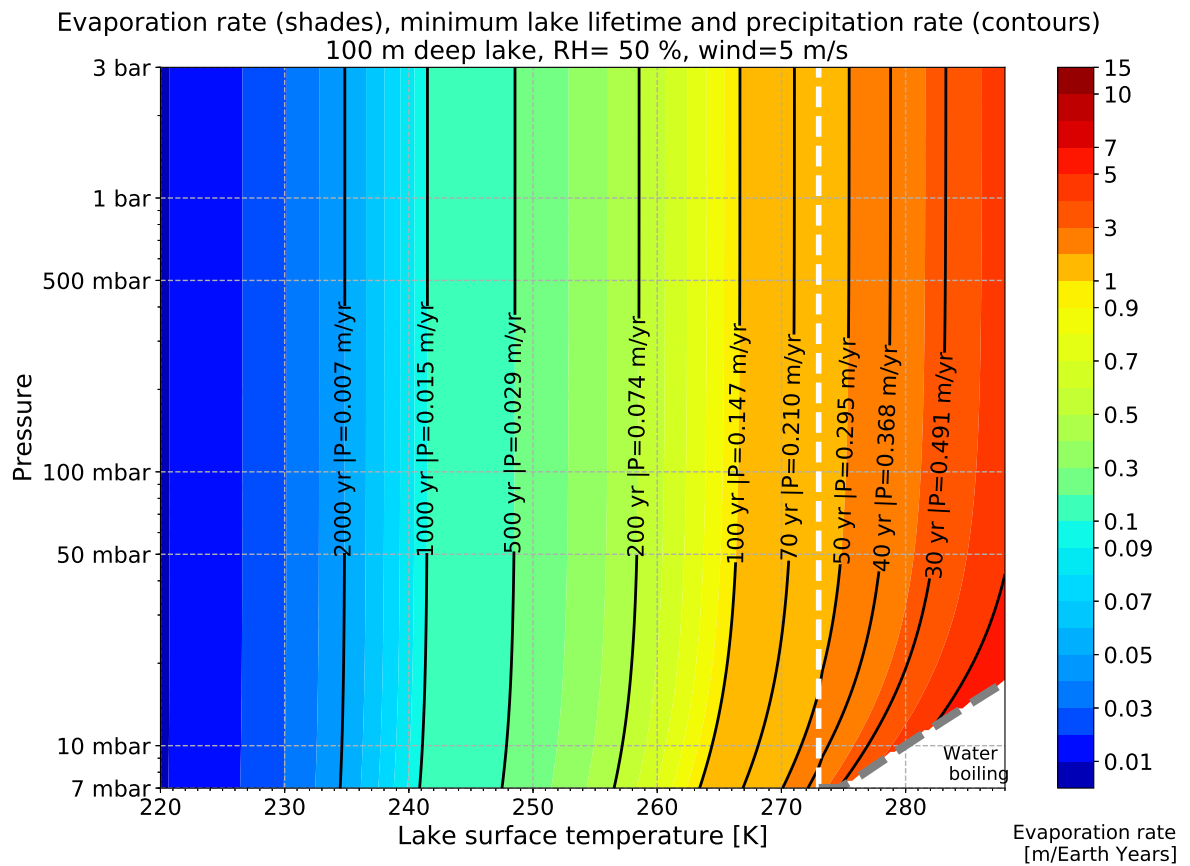


Figure 3: Evaporation rate (shades), minimum lifetimes for a 100m deep lake and precipitation rates required to sustain the water level (black contours) as a function of the pressure and temperature. The white dashed line shows 273K.

(arbitrary) atmosphere at $T=273\text{K}$, $P=500\text{ mbar}$, $\text{RH}=50\%$ and different values for the surface wind speed and run-off coefficient.

Figure 3 shows that for any pressure ranging between 7 mbar and 3 bar, an open water lake (i.e an annually averaged regional surface temperature $\overline{T_R} > 273\text{K}$) will evaporate in less than 60 Earth years if not resupplied by some processes such as rain fall, snow melt, or groundwater flows. A direct consequence is that for these ranges of pressures and temperatures, a hydrological cycle is required to sustain open water lake conditions over a long period of time ($>10,000$ years). For cold climates ($\overline{T_R} \ll 273\text{K}$) the lakes last longer without precipitation (in the order of hundreds to thousands of years), or alternatively maintain their levels constant with smaller precipitation rates (a few millimeters to a few centimeters per year).

When the temperature $\overline{T_R}$ is 273K and for a run-off coefficient of 20%, Table 2 shows that the precipitation rate estimates at Gale crater are in the order of a few tens of centimeter per year. These values lie toward the upper limit for the rainfall estimates required to form the valley networks during the Noachian (less than 1 mm yr^{-1} to $\sim 1.1\text{ m yr}^{-1}$ Von Paris et al. (2015)), and for reference, are similar to the range of those for the American southwestern states (NOAA, 2015). Ultimately this simple calculation only confirms the intuitive guess that in order to have Earth-like open water lakes on Mars, there is a requirement for high (Earth-like) rainfalls rates. Such high precipitation rates may be challenging to reconcile with the relatively low erosion at that time when compared to the Earth. Estimates for the erosion rates averaged over the entire Hesperian are $0.02\text{--}0.03\text{ nm yr}^{-1}$ (Golombek et al., 2006) and those for the Earth are $10^4 - 10^5\text{ nm yr}^{-1}$ (Carr and Head, 2010). Another challenge with open water lakes in equatorial regions is that they may require large bodies of open water to power the hydrological cycle (e.g. a lake in Eridania basin Irwin et al. (2002) or a northern ocean Haberle et al. (2017); Clifford and Parker (2001); Clifford and Costard (2017)). The implication would be that the temperatures must have been above the freezing point not only at equator, but also at higher latitudes so these large reservoirs would have also remained unfrozen.

In the following section, we test the existence of open water lakes conditions by considering if first the annually-averaged *global* mean temperature, second the annually-averaged *equatorial* temperature and third the equatorial *seasonal* temperature could have been above the freezing point.

3. Temperature requirements for open water lakes

Annually-averaged global mean temperature

The simplest, yet most informative way to reproduce the Martian surface temperatures, or those of any other planetary body, is to compute the planetary equilibrium temperature T_{eq} which represents the equilibrium temperature of a planet needed to balance the absorbed solar flux received from the sun in the absence of an atmosphere:

$$\underbrace{(1-a)\varphi_0\pi R^2}_{\text{received from sun}} = \underbrace{\epsilon\sigma T_{eq}^4 4\pi R^2}_{\text{emitted to space}} \Rightarrow T_{eq} = \sqrt[4]{\frac{\varphi_0(1-a)}{4\epsilon\sigma}} \quad (6)$$

with $a \approx 0.25$ the planetary albedo, $\varphi_0 = \frac{1370\text{Wm}^{-2}}{1.52^2} \approx 600\text{Wm}^{-2}$ the solar flux at Mars, πR^2 the planet's cross section with $R=3390\text{ km}$ the planet's radius, $\epsilon \approx 1$ the emissivity, $\sigma = 5.67 \times 10^{-8}\text{Wm}^{-2}\text{K}^{-4}$ the Stefan constant and $4\pi R^2$ the surface area for the planet. The difference between the equilibrium temperature T_{eq} and the effective (measured) surface temperature of the planet T_{se} is attributed to greenhouse warming from the atmosphere. For the Earth, the greenhouse warming is about 33K , but for present-day Mars, it is on the order of a few kelvin only (see discussion in Haberle (2013)). This may seem counter-intuitive, as the column amounts of CO_2 are ≈ 40 times greater on Mars than they are on Earth. However the saturation of the main ($15\ \mu\text{m}$) absorption band, the low atmospheric pressure (i.e weak pressure broadening) and the limited presence of other greenhouse gases, such as water vapor, make overall greenhouse warming less effective on Mars (Read et al., 2015). During the period of deposition at Gale crater, $\sim 3.6\text{ Gya}$, stellar evolution models predict that the sun was about 75% as bright as at present (faint young sun, Gough (1981); Kasting (1991); Bahcall et al. (2001)). Using this reduced value of incoming solar flux and the same value for the planetary albedo, the equilibrium temperature T_{eq} from Eq. (6) drops to $\approx 196\text{K}$ implying that $\sim 77\text{K}$ of warming are needed to explain the presence of liquid water during the Hesperian ($\overline{T_G}=273\text{K}$).

Recent estimates for ancient surface pressure on Mars range from a few tens of mbar (Bristow et al., 2017), possibly more if groundwater infiltration was occurring (Tosca et al., 2018), to approximately a bar (Barabash et al., 2007; Leblanc and Johnson, 2002; Edwards and Ehlmann, 2015; Kite et al., 2014; Jakosky et al., 2017; Hu et al., 2015). However, limiting the early Mars paradigm to the $\text{CO}_2/\text{H}_2\text{O}$ inventory alone is not sufficient, and Kasting

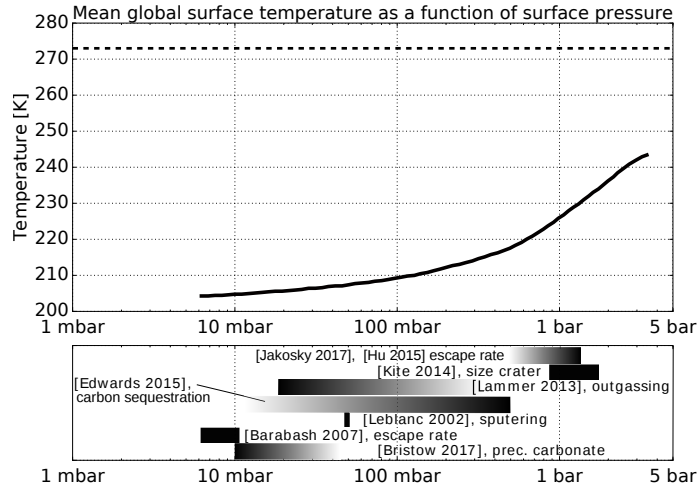


Figure 4: (top) Surface mean temperature as a function of surface pressure for a $\text{CO}_2\text{-H}_2\text{O}$ atmosphere, adapted from Kasting (1991)’s 80 % solar luminosity case. (bottom) Surface pressure estimates for early Mars derived from various methods.

(1991) demonstrated using a convective-radiative model that because higher pressures facilitate the condensation of CO_2 , even 10 bars of CO_2 will not warm the atmosphere nearly close to the freezing point of water (see Figure 4). Many modeling studies have attempted to remedy Kasting (1991)’s findings by including the effects of collision-induced absorption (CIA) and far-line absorption by CO_2 molecules (Wordsworth et al., 2010), using three dimensional simulations to model the radiative effects of CO_2 clouds (Forget et al., 2013), water ice clouds (Wordsworth et al., 2013), and dust (Kahre et al., 2013), simulating transient heating through impact craters (Segura et al., 2012; Steakley et al., 2019), testing the warming effects of sulfur dioxide (volcanism, Havelly and Head (2014)), H_2 -driven greenhouse warming (Ramirez et al., 2014; Wordsworth et al., 2017), carbonate-silicate limit cycles (Batalha et al., 2016), and outgassing of methane (Kite et al., 2017). To date, finding ways to produce such an important warming remains one of the major challenges in planetary science, in the absence of an obvious mechanism for either transient or long-lived greenhouse atmospheres (Wordsworth, 2016; Haberle et al., 2017).

Annually-averaged equatorial temperature

In place of reducing the early Mars paradigm to a globally-averaged temperature requirement, we can assess whether the conditions for liquid water can be met locally. Because the orbital parameters for Mars are known to have changed over time (Laskar et al., 2002), and since the atmospheric inventory during the Hesperian remains poorly constrained, we will use analytical formulations when possible so our calculations may be repeated for different climate scenarios. The simplest way to estimate the regional temperature is to use a latitudinally-resolved energy balance model (EBM) to capture, at least to a first order, the dependence of the local energy balance on the latitude. Such models have been used for *numerical* climate studies of Mars (e.g. Postawko and Kuhn (1986), Hoffert et al. (1981), Williams and Kasting (1997)). In this paper though, we adapt one of the original methods by North (1975a) to provide an *analytical* solution for the annually-averaged surface temperature for early Mars for different surface pressure, eccentricity and obliquity scenarios. The reasoning for the energy balance model is similar to the equilibrium temperature calculation in Eq. (6) where we said that globally, the absorbed solar radiation is balanced by the longwave flux emitted radiatively by the surface. The addition of an atmosphere to this framework has the following effects: First, the outgoing longwave radiation (OLR) radiated to space is not equal the surface blackbody radiation anymore (σT_{sfc}^4) but is now dependent on the radiative properties of the atmosphere (e.g. mass of the atmosphere, presence of greenhouse gases, clouds). Second, the atmosphere can transport diffusively the excess of heat (generally poleward) when the incident solar radiation and the OLR are unbalanced. Let E be the energy in an atmospheric column and assume that variations of E can be related to variations of the surface temperature T_s . Following Hoffert et al. (1981), we have:

$$\begin{aligned} \frac{\partial E}{\partial t} &= (1 - a(\Phi)) Q_{sun}(\Phi) - OLR(\Phi) \\ &+ \frac{D}{\cos(\Phi)} \frac{\partial}{\partial \Phi} \left(\cos(\Phi) \frac{\partial T_s}{\partial \Phi} \right) \end{aligned} \quad (7)$$

with a the planetary albedo, Q_{sun} the incident solar radiation, OLR the outgoing longwave radiation at the top of the atmosphere, D the eddy diffusivity coefficient for the meridional transport and T_s the surface temperature. Note that a , Q_{sun} and the OLR are all dependent on the latitude Φ . A convenient approximation is to assume that the OLR varies linearly with the surface temperature (more about this approximation below and in Figure 5):

$$OLR = A + B T_s \quad (8)$$

with A and B two parameters to be determined for different atmospheric compositions and surface pressures. Setting the variable $x = \sin(\Phi)$, averaging Eq. (7) over one Martian year (i.e. $\frac{\partial E}{\partial t} \approx 0$) and re-organizing the terms lead to:

$$\begin{aligned} D \frac{d}{dx} \left((1 - x^2) \frac{d\overline{T}_s(x)}{dx} \right) - (A + B \overline{T}_s(x)) = \\ - (1 - \overline{a}(x)) \overline{Q}_{sun}(x) \end{aligned} \quad (9)$$

which is a differential equation for the surface temperature $\overline{T}_s(x)$, the overbars denoting yearly-averaged values. In the particular case where the shortwave term $(1 - \overline{a}(x)) \overline{Q}_{sun}(x)$ in Eq. (9) is approximated as a series of even Legendre polynomials, North (1975a) showed that an analytical solution of Eq. (9) exists and he provided a solution for the Earth with integration constants that depend on the boundary conditions at poles and at the equator. We adapted the solution of North (1975a) to Mars in the special case where the albedo is a continuous function of the latitude, and we show in the Appendix that the annually-averaged temperature is:

$$\begin{aligned} \overline{T}_s(x) &= \frac{\varphi_0}{4 \sqrt{1 - e^2}} \left(\frac{Sa_0}{B} \right) - \frac{A}{B} \\ &+ \frac{\varphi_0}{4 \sqrt{1 - e^2}} \left(\frac{Sa_2 p_2(x)}{6D + B} + \frac{Sa_4 p_4(x)}{20D + B} \right) \end{aligned} \quad (10)$$

with x the sine of the latitude, φ_0 the solar constant at Mars (e.g. $\frac{1370}{1.52^2} W.m^{-2}$ for present day), e the eccentricity, D the diffusivity of the atmosphere, A and B the OLR parameters as in Eq. (8), Sa_n the insolation parameters provided in the Appendix and $p_n(x)$ the Legendre polynomials. The diffusivity D is estimated following Hoffert et al. (1981):

$$D \sim 0.058 \left(\frac{p}{1013} \right) \Delta \overline{T}_m \quad [Wm^{-2}K^{-1}] \quad (11)$$

with p the surface pressure in unit of mbar and $\Delta \overline{T}_m$ the temperature difference between the poles and the equator. For present-day Mars ($p=7$ mbar), $\Delta \overline{T}_m \approx 55K$ leads to $D \sim 0.02 Wm^{-2}K^{-1}$. For an ancient, heavier, atmosphere we expect a stronger meridional transport (D increases) because the atmosphere would re-distribute the heat more efficiently and therefore the temperature gradient $\Delta \overline{T}_m$ would decrease. The former is unknown a priori but we can use a numerical solver to find values for D and $\Delta \overline{T}_m = \overline{T}_s(1) - \overline{T}_s(0)$ that satisfy both Eq. (9) and Eq. (11). We found that the diffusivity D ranges from 0.08 to 1.36 $Wm^{-2}K^{-1}$ for 50 mbar- 4 bar atmospheres with present-day obliquity, and values for D are given in Table 3 in the Appendix as a function of the surface pressure. We emphasize that since in our simple model, just about everything of what is currently known of the Martian atmosphere's dynamics is reduced to a single diffusivity parameter D , Eq. (11) is an order-of-magnitude estimate only. For a 1 bar atmosphere, this method gives $D=0.70 W/m^2/K$, which is 1.2-1.8 times the estimated value for the Earth at 1 bar ($D = 0.38-0.58 Wm^{-2}K^{-1}$ North (1975b); Williams and Kasting (1997)) and consistent with the scaling method proposed by Williams and Kasting (1997).

Integrating Eq. (10) latitudinally across one hemisphere (x ranging 0 to 1) and evaluating the function near the equator ($x \approx 0$) provides estimates for the annually-averaged global mean temperature \overline{T}_G and the annually-averaged regional temperature near Gale's latitude \overline{T}_R :

$$\left\{ \begin{array}{l} \overline{T}_G = \frac{1}{B} \left(\frac{\varphi_0}{4\sqrt{1-e^2}} Sa_0 - A \right) \\ \overline{T}_R = -\frac{A}{B} + \frac{\varphi_0}{4\sqrt{1-e^2}} \left(\frac{Sa_0}{B} - \frac{1}{2} \frac{Sa_2}{6D+B} \right. \\ \left. + \frac{3}{8} \frac{Sa_4}{20D+B} \right) \end{array} \right. \quad (12)$$

At this point, the missing parts of our climatic puzzle are the planetary albedo $\overline{a}(x)$, and the longwave parameters A and B that are used to estimate the outgoing longwave radiation. The OLR is strongly dependent on the surface pressure, the thermal structure of the atmosphere, the presence of condensable species (H_2O or CO_2 clouds), and the vertical distribution of radiatively active species (e.g. dust, water vapor, H_2 , CH_4), which are all poorly constrained for early Mars. The effects of water ice clouds and CO_2 clouds on the longwave radiative budget (potentially positive feedback on the surface temperature) and on the planetary albedo (negative feedback on the surface temperature as more solar energy is reflected) are not included. Under these assumptions, we found that adding small amounts of water vapor (a few tens to hundreds of precipitable μm) in contrast to the much bigger water inventories used in other studies, (e.g. 13.3 m global equivalent layer of water in Segura et al. (2012)) had little influence on the radiation budget for the range of surface temperatures considered ($\sim 200\text{K}$ - 273K) thus we assume a pure CO_2 atmosphere. Methods to estimate the radiative fluxes range in complexity from analytical single-band gray radiative models (as in Robinson and Catling (2012)), to computationally expensive line-by-line radiative codes (as in Wordsworth et al. (2017)). Some parameterization for the atmosphere's dynamical response to the radiative forcing may be included, for instance through a convective adjustment or by explicitly resolving advection and mixing, as it is the case in Global Climate Models (GCMs). For our purposes (linear fit of the OLR as a function of the surface temperature: $OLR = A + B T_s$), a rough estimate for the OLR is sufficient. For simplicity, we construct a range of heuristic, annually-averaged, temperature profiles for different surface pressures and annual mean surface temperatures by simply following the dry adiabatic lapse rate ($\sim 4.7\text{K}/\text{km}$) and ensuring that the temperatures stay above the CO_2 condensation curve at all heights. Fictive temperature profiles for a cold case ($\overline{T}_R=220\text{K}$) and a warm case ($\overline{T}_R=270\text{K}$) are illustrated as dashed lines in Figure 5 (left) and compared with the yearly-averaged prediction from a three-dimensional, fully interactive, GCM simulation with a 1 bar atmosphere and reduced solar luminosity (solid grey line). The fictive temperature profiles present the same general structure as the one predicted by the GCM, with an Earth-like troposphere and temperature gradually decreasing with height due to the increased efficiency of convective heat transport (mixing) at high pressures. This situation differs from present-day Mars (yearly-averaged values for a present-day, 7mbar GCM simulation are shown as a solid black line in Figure 5 (left)) where the vertical temperature structure varies widely as a function of the season and the local time (Savijarvi, 1999). The outgoing longwave radiation flux at the top of the atmosphere $Q_{IR\uparrow}^{TOA}$ and the downward infrared flux at the surface $Q_{IR\downarrow}^{sc}$ are obtained by running the NASA Ames radiation code for each of these static temperature profiles, including the effects of the infrared collision-induced absorption (CIA) and the far-line absorption at high pressure following Wordsworth et al. (2010). Figure 5 (top right) compares OLR estimates retrieved from the fictive profile method with OLR values from three-dimensional, fully interactive, GCM simulations for the 7mbar (present-day) atmosphere and the 1 bar atmosphere with reduced solar luminosity. The OLR values from the GCM simulations (markers) are more dispersed than what the fictive profiles can account for since, for identical values for the surface temperature, air temperature inversions are not captured by the static profiles. However, the slopes for the OLR retrieved from the static profiles (dashed lines) match reasonably well the best fits to the GCM's outputs (solid lines). While being overly simplistic (the temperature structure is only an educated guess), this approach does capture the effect of increasing surface pressure and increasing atmospheric temperature on the longwave radiative budget. Similarly, global mean values for the planetary albedo a_0 are retrieved from the radiative transfer calculation as a function of the surface pressure and are averaged over all the solar zenith angles, assuming a surface albedo of 0.2. As it is instructive to account for the dependence of the albedo on the latitude, we provide an optional fitting factor f_a that correlates high albedo values to high solar zenith angles (i.e. low mean annual solar insolation), does not alter the global mean value (the integral of $\overline{a}(x)$ over all latitudes is equal to a_0), and can be easily incorporated in the shortwave term of Eq. (9) (see bottom right panel in Figure 5, and the discussion in the Appendix).

We now have all the necessary tools to reproduce the first order, yearly-averaged climatology on Mars for different surface pressures. First, results from the analytical climate model are compared with those from the NASA Ames GCM for present-day Mars. The Nasa Ames GCM integrates a two-stream radiative transfer code,

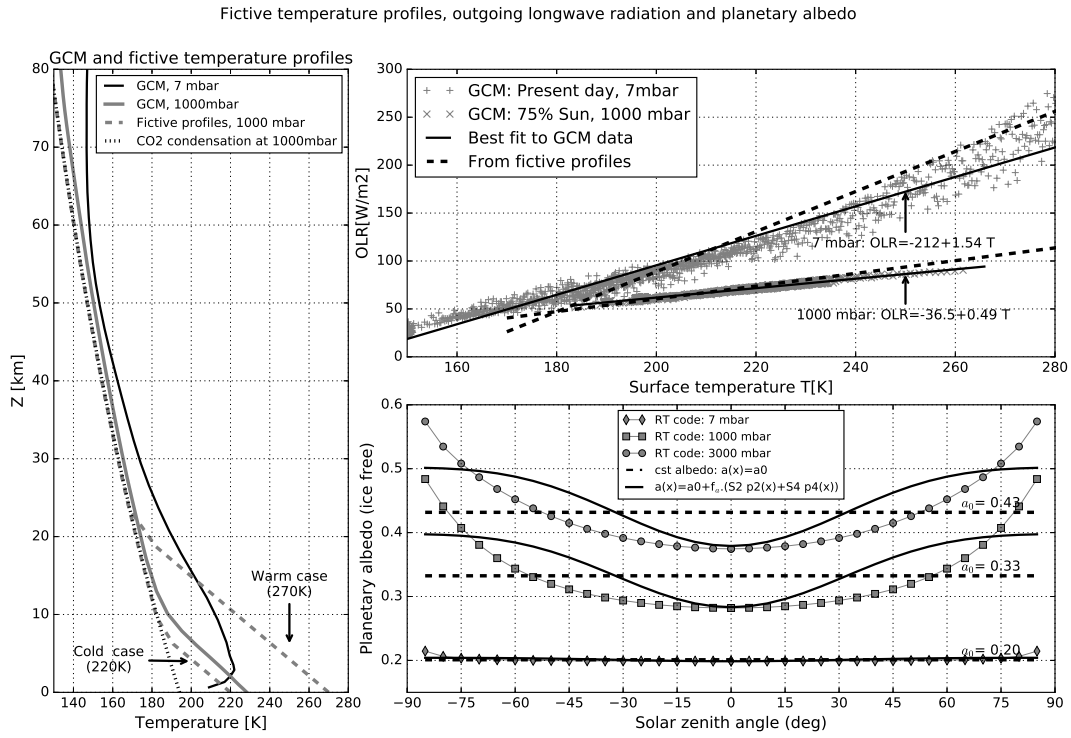


Figure 5: (Left) Warm case and cold case fictive temperature profiles for a 1000 mbar pure CO₂ atmospheres (grey dashed lines). The CO₂ condensation curve for a 1000 mbar atmosphere (thin dotted line) shows how the profiles are constructed. Temperature profiles from full three-dimensional GCM simulations (year-average) are shown for reference for a present-day 7mbar atmosphere and a 1000 mbar ancient atmosphere (solid lines, see [Smith et al. \(2017\)](#) for others examples of temperature profiles derived from both modeling and observations). (Top right) Outgoing longwave radiation at the top of the atmosphere derived from the fictive temperature profiles and from the three-dimensional GCM simulations for the 7mbar and the 1000 mbar atmosphere. (Bottom right) Albedo as a function of the solar zenith angle (or equivalently as a function of the latitude for a 0° obliquity) for different surface pressures, are retrieved from the radiative transfer code (markers). The constant albedo model (dashed lines) and mean solar insolation-weighted model (solid lines) described in the Appendix are also shown.

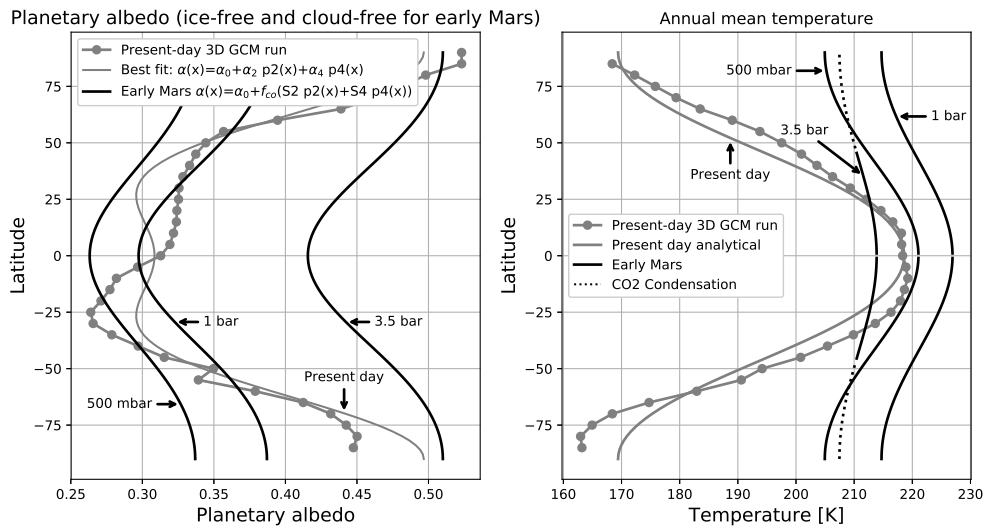


Figure 6: (Left) Zonally-averaged planetary albedo from the 7mbar GCM simulation (grey markers), best fit for present-day Mars (grey symmetrical line with respect to the equator) and albedo distribution used for the early Mars predictions (black lines). (Right) Comparison of the mean annual temperature predicted by the NASA-Ames GCM (grey markers) with the analytical model for present-day Mars (grey line), and analytical predictions for early Mars for different surface pressures (black lines).

explicit 3D modeling of the atmospheric circulation, and a much more accurate representation of the aerosols and interactions between the surface of the atmosphere (see [Haberle et al. \(2019\)](#) for model updates). OLR values are retrieved from a 7 mbar GCM simulation (atmospheric dust and clouds are radiatively active), and fitted as a linear function of the surface temperature: $OLR = -212 + 1.54 T_s$ (see Figure 5, top right). The diffusivity is $D \sim 0.02 W m^{-2} K^{-1}$, and we provide a direct fit to the NASA Ames General Circulation model for the annual mean, zonally-averaged planetary albedo:

$$\begin{cases} \bar{a}(x) = a_0 + a_2 p_2(x) + a_4 p_4(x) \\ a_0 = 0.329 \quad a_2 = 0.0954 \quad a_4 = 0.0721 \end{cases} \quad (13)$$

with x the sine of the latitude, $p_n(x)$ the even Legendre polynomials. Note that the asymmetrical "W-shape" of the planetary albedo distribution retrieved from the GCM (grey markers in Figure 6 (left)) can be related to Mars' surface albedo (refer to albedo maps by [Christensen et al. \(2001\)](#)), the annual deposition of CO₂ ice at high latitudes, and the distribution of clouds predicted by the GCM. All together, these processes lead to a yearly-averaged global mean value for the planetary albedo of ~ 0.3 , which is higher than the albedo obtained with the fictive profile method ($a_0 = 0.2$ at 7mbar in Figure 5 (bottom right)). This means that the albedo values used in the latitudinally-resolved energy balance model are favorable (low) to produce warm surface temperatures. Figure 6 (right) shows that, despite its simplicity, the analytical climate model (grey line) reproduces remarkably well the annually-averaged surface temperature from the GCM for present-day Mars (grey markers and line). The temperatures predicted are almost identical to the GCM at the equator, typically 5-7K colder than the GCM at mid latitudes and slightly warmer than the GCM at the poles. Since only even Legendre polynomials are used to describe the distributions for the albedo and the solar insolation, the temperatures predicted by the analytical model are symmetrical with respect to the equator and can be seen as the average value of both hemispheres.

The analytical model was then used to investigate different surface pressure, obliquity and eccentricity scenarios for early Mars. As an example, for a 1 bar, early Mars case, the luminosity φ_0 is reduced by 75%, we read in Table 3: $D \sim 0.70 W m^{-2} K^{-1}$, $A = -72$, $B = 0.66$, $\alpha_0 = 1 - 0.33$ and $f_{co} = +0.135$ (see Appendix). Seasonal variations in temperatures are not considered in the annually-averaged EBM so the stability of the atmosphere against atmospheric collapse is not ensured but we can at least test the annual mean surface temperatures against the condensation temperature of CO₂ to check for the formation of perennial ice caps. The expression from [Forget et al. \(2013\)](#); [Fanale et al. \(1982\)](#) for the condensation temperature of CO₂ is repeated here for convenience:

$$T_{cond} = \frac{-3167.8}{\ln(0.01 * P) - 23.23} \quad [K] \quad (14)$$

with P the pressure in Pa and $P \lesssim 5$ bars.

Figure 6 (left) shows the planetary albedo (ice-free and cloud free Mars) and annually-averaged surface temperatures (right) for a 500mbar, 1 bar and 3.5 bar atmospheres using present-day orbital parameters and 75 % reduced solar luminosity (black lines). For the 500 mbar atmosphere and for the 1 bar atmosphere, greenhouse warming and rather low values for the planetary albedo lead to surface temperatures warmer than present-day, despite a faint young sun (black lines in Figure 6 (right)). However, further increasing the surface pressure to 3.5 bar ultimately results in lower surface temperatures. This is due to atmospheric scattering at high pressure that increases the planetary albedo (left panel in Figure 6) beyond what greenhouse warming can compensate for. Furthermore, surface temperatures beyond 50 degrees of the equator for the 3.5 bar case drop below the condensation temperature of CO₂ (dotted lines in Figure 6 (right)) so this solution is not stable against atmospheric collapse, consistently with the upper limit for stable atmospheres of ~ 3 bar described in [Forget et al. \(2013\)](#). Using lower values for the obliquity and higher values for the eccentricity (not shown) raises the annually-averaged equatorial temperature by a few kelvin (up to $\sim 235K$ for a 2 bar atmosphere) but we found that there is no obvious combinations of orbital parameters that would lead to annually-averaged equatorial temperature \bar{T}_R above 273K. There are two main reasons for this: First, increasing the eccentricity e increases the energy received by the whole planet (note the $\sqrt{1 - e^2}$ factor in the denominator of Eq. (12) and see discussion in [Berger and Loutre \(1994\)](#)), but this effect is minor: the planet experiences warmer temperatures near perihelion, colder temperatures near aphelion and the integrated effect over an entire year is small. Second, we notice that the meridional gradient in temperature decreases significantly with increasing pressures (compare the pole-to-equator temperature differences between the 7 mbar case and the 1 bar case in Figure 6 (right)). This is again due to the increased efficiency in diffusive heat transport, that better redistributes heat across all latitudes for high surface pressures (D increases in Eq. (12)). As a result, although changes in obliquity do impact the latitudinal distribution in temperature, they do so to a much

lesser extent than would be the case for Amazonian (low surface pressure) climates. Therefore, we use present-day values for the orbital parameters for the rest of this study. The global effects of clouds, water vapor, or other reduced greenhouse gases on the longwave radiative budget are not included in this study but could easily be incorporated into the parameters A and B ¹. Admittedly, several approximations in this model could be improved (e.g. better parameterization for the planetary albedo as a function of the latitude, use of self-consistent vertical temperature profiles, address the seasonal formation of ice caps), especially if the energy balance in Eq. (7) is solved numerically. Yet, the analytical model is consistent with other GCM studies in predicting cold climates: For example [Wordsworth et al. \(2013\)](#) and [Forget et al. \(2013\)](#) found that the annual mean temperatures for equatorial regions peak from $\overline{T_R} \sim 230\text{K}$ ($\overline{T_G} \sim 210\text{K}-215\text{K}$) for 0.2-0.5 bar simulations to $\overline{T_R} \sim 245\text{K}$ ($\overline{T_G} \sim 230\text{K}$) for 1-2 bar simulations. This suggests that the surface of the lakes at Gale crater during the Hesperian must have been frozen, at least for part of the year.

Seasonal maximum for the equatorial temperature

To assess if seasonal melting of the frozen lake occurred, we compute the seasonal variations in temperature that equatorial regions may have experienced. Following [Dundas and Byrne \(2010\)](#); [Hecht \(2002\)](#); [Kite et al. \(2013\)](#); [Mansfield et al. \(2018\)](#), we use a computationally inexpensive one-dimensional numerical model with a single, parameterized, atmospheric layer and write the energy balance at the surface as:

$$\frac{\partial U}{\partial t} = (1 - a)Q_{sun\downarrow}^{TOA} + Q_{IR\downarrow} + Q_{cond} + Q_{geo} + SH - \epsilon\sigma T_{surf}^4 \quad (15)$$

with U the energy per unit of area for the surface layer, a albedo combining the reflection from the atmosphere and the ground (we use the constant value a_0 from Table 3 in the Appendix as the average over all zenith angles), $Q_{sun\downarrow}^{TOA}$ the shortwave radiation at the top of the atmosphere and equal to 75% of its present-day value, $Q_{IR\downarrow}^{sf}$ the downward longwave radiation from the atmosphere, Q_{cond} the conductive flux through the surface, Q_{geo} the geothermal flux, $\epsilon\sigma T_{surf}^4$ the longwave upward radiation, and SH the sensible heat lost to the atmosphere. All the terms from Eq. (15) are described in the Appendix, as well as the physical parameters (e.g wind speed) chosen in the calculation. Note that the energy balance in Eq. (15) is applied to the surface layer this time, and not to the entire atmospheric column as in Eq. (7). With the visible atmospheric optical properties incorporated into the albedo a , almost of all the terms in Eq. (15) are either related to the surface layer itself (e.g. conduction to the ground, radiative losses) or to the atmospheric layer immediately adjacent to the surface (e.g. sensible heat flux). The only exception is $Q_{IR\downarrow}^{sf}$ that depends on the temperature structure through the entire atmospheric column. We use a constant value $Q_{IR\downarrow}^{sf}(\overline{T_R})$ with $\overline{T_R}$ derived from the analytical model (Eq. (12)) and we provide a parameterization for $Q_{IR\downarrow}^{sf}$ in Table 3 as a function of the surface pressure. As we are interested in the regional average values, the soil is assumed to be dry (no water/frost) so the ground properties are representative of the Martian regolith and there is no latent heat terms. The time-stepping model in Eq. (15) was tested against predictions from the NASA Ames GCM for present-day Mars and reproduced reasonably well the surface temperatures from the Ames GCM: over a full Martian year, the annually-averaged surface temperature at Gale crater $\overline{T_R}$ was 223K both models and the daily-averaged temperature from the one dimensional model was no more than 3K different than the GCM's at any time of the year. The one dimensional model also reproduced adequately the phase and amplitude of the diurnal ground temperature variation (peak afternoon temperatures and nighttime temperatures were within 5K of those predicted by the GCM), in agreement with ground temperature measurements from the *Curiosity* rover (see [Martínez et al. \(2017\)](#) for a overview of ground temperature data as a function of the local time).

Then, we ran the time-marching model with different values for the surface pressure and a reduced solar luminosity. Consistently with the predictions from the analytical climate model, we verified that changes in obliquity and eccentricity only resulted in warmer/colder departures from an annual mean value that was tens of kelvin below 273K. Therefore we keep present-day orbital parameters for simplicity and focus instead on the effects of the surface pressure on the amplitudes of the diurnal and seasonal variations in surface temperature.

Figure 7 confirms that annual mean surface temperatures $\overline{T_R}$ (black lines) increase with increasing pressure as the atmosphere provides more greenhouse warming, up to a certain point where the increase in albedo (atmospheric scattering) limits this effect ($\overline{T_R}$ does not increase much from 1 bar to 2 bar). The time-stepping calculation shows that the seasonal maximum temperature (e.g average temperature for the hottest day of the year, shown as the upper parts of the grey bars in Figure 7) are well below the freezing point (dashed line at 273K). This means that not only

¹the radiative transfer solver used in this study is freely available on the NASA Ames Mars Climate Modeling Center's website

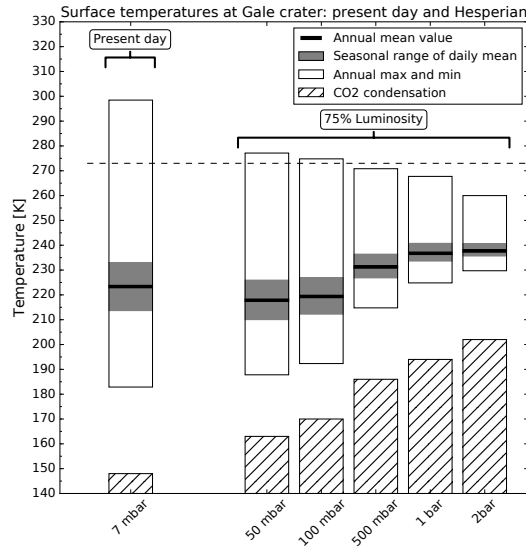


Figure 7: Estimates for the annually-averaged regional temperature near Gale’s latitude (thick black lines), seasonal variation of the daily-averaged temperature (grey bars), yearly temperature maximum and minimum (white bars) and condensation temperature of CO₂ (hatched bars) from the time-stepping model for different surface pressures.

the baseline state (year-average) for the lakes was frozen, but furthermore the lakes must have been *perennially* ice-covered. However, not unlike present-day Mars, peak daytime temperatures (e.g temperature for the hottest hour of the year, shown as the upper parts of the white bars in Figure 7) do get above 273K for the moderate pressure cases (<500mbar). Note that increasing the surface pressure tends to decrease the daily and the seasonal ranges of temperature (respectively white and grey bars in Figure 7), toward a less extreme, Earth-like configuration where convective eddies efficiently cool the radiatively-heated surface during the day (see Eq. (48) in the Appendix and Rafkin et al. (2013)). The general trend is that low to moderate surface pressures ($P < 500$ mbar) result in cold mean temperatures ($T \ll 273$ K) but large seasonal and daily excursions from the mean, and high surface pressures ($P > 500$ mbar) result in slightly higher mean values but smaller daily and seasonal excursions from the mean.

To summarize, we consistently demonstrated that there is no combination of surface pressure and orbital parameters that could have led to either permanent or seasonal open water lakes at Gale crater during the Hesperian. Our best estimates for the equatorial temperature falls short of at least 30K to the freezing point, using pure ice as a limiting case (absent of salt). Since climate studies have consistently predicted a cold climate for early Mars (Haberle et al., 2017; Wordsworth, 2016), we propose to investigate the cold and wet scenario where lakes created during the Noachian could have persisted in the form of perennially ice covered-lakes.

4. The ice-covered lakes hypothesis

Analogy with perennially ice-covered lakes in Antarctica

In the Dry Valleys of Antarctica, the annual mean temperatures are below freezing, yet sustained liquid water occurs under perennial ice covers (Armitage and House, 1962; Doran et al., 1994; Sokratova, 2011). These perennially ice-covered lakes occur in topographic lows and are either isolated or abutted by glaciers. The seasonal melting of snow and/or glacial meltwater recharges the liquid water column of the lakes and provides a source of energy in the form of latent heat. The thickness of the ice cover is set by the energy balance and by the mass balance of the ice cover, ice being removed by ablation at the surface and added to the bottom by freezing (McKay et al., 1985). Two different types of perennially ice-covered lakes are possible analogues for the lake that could have been present in ancient Gale crater: 1) lakes that are recharged entirely by inflowing melt streams, such as the lakes in the McMurdo Dry Valleys and 2) lakes that have significant recharge from subaqueous melting of abutting glaciers, such as Lake Untersee (Steel et al., 2015; Faucher et al., 2019). Sedimentary structures have been documented at the bottom of both types of lakes (Simmons et al., 1987; Squyres et al., 1991; Levitan et al., 2011). For the McMurdo Dry Valleys lakes, maximum air temperatures above freezing (expressed as degree-day above freezing) are

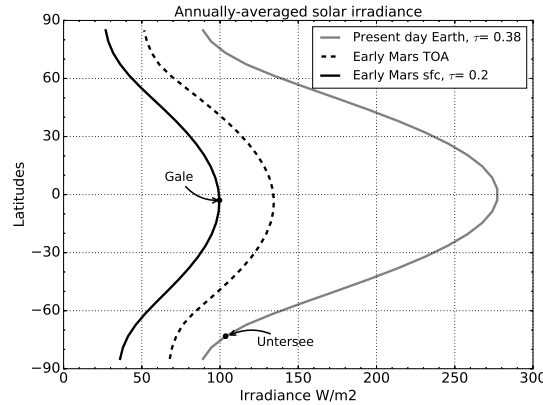


Figure 8: Annually-averaged surface solar irradiance as a function of latitude for early Mars and present-day Earth under clear sky conditions. The irradiance at the top of the atmosphere (TOA) and at the surface for a visible optical depth $\tau=0.2$ are shown for Mars and $\tau = 0.38$ is used for Earth. (See Liu and Jordan (1960) for a simple parameterization for the diffuse radiation for the Earth)

required in summer for meltwater to flow into the lake. Applying this analogue to Mars, McKay and Davis (1991) explored the idea that sustained liquid water could have been persisted long after the global mean temperature fell below freezing. In their study, the requirement for long-lasting lakes was that the peak seasonal temperatures exceeded the freezing point of water. Under these conditions, they found that sustained liquid water on Mars could have been preserved for 100's of millions of years after the global mean temperature fell below the freezing point.

Lake Untersee, East Antarctica, has a surface area of 11.4 km². It is sealed by a ~ 3m perennial ice cover and dammed by the Anuchin Glacier (Andersen et al., 2011; Wand et al., 1997; Steel et al., 2015; Faucher et al., 2019). The annual mean air temperature is -10.6C° (Andersen et al., 2015) The bottom of Lake Untersee is dominated by clay-sized sediment (although larger grains have been documented) and the mud in the lake is primarily derived from the abutting glacier (Steel et al., 2015; Faucher et al., 2019). At Lake Untersee, solar radiation penetrates the ice cover and melts the glacier's wall underneath the lake's surface, recharging the lake in meltwater. As a follow-up study of McKay and Davis (1991) and FairË'n et al. (2014) in which glacial and periglacial activity is present, we propose to investigate the Lake Untersee model for Gale crater because it does not requires liquid water to flow at the surface at any time of the year. While this model alone may not explain all of the sedimentary deposits encountered by the Curiosity rover (e.g. river deposition), it provides a starting point for exploring the range of possible lake scenarios for Gale crater during the Hesperian that are consistent with climatic studies.

Solar radiation and the ice albedo are key parameters allowing for the preservation of ice-covered lakes in below-freezing temperatures (McKay et al., 1985; McKay, 2004). Since the values for the albedo given in Table 3 already include reflection by the ground, the reduction in solar insolation due to atmospheric reflection is conveniently defined through a mean visible optical depth τ in order to differentiate the effects of the atmosphere from the effect of the local ice on the solar energy available at the surface:

$$Q_{sun\downarrow}^{sfc} = Q_{sun\downarrow}^{TOA} e^{-\tau} \quad (16)$$

Following Levine et al. (1977); Hottel (1976); Liu and Jordan (1960), we show in Figure 8 the annually-averaged clear sky solar irradiance at the surface as a function of latitude for early Mars with present-day orbital parameters, and for present-day Earth (we use a visible optical depth $\tau = 0.2$ for a 500 mbar atmosphere). The annually-averaged solar irradiance at Gale crater and at Lake Untersee are comparable: the faint young sun and the greater sun-Mars distance result in a reduction of the solar irradiance with respect to present-day Earth by a factor of 3 (we have $0.75 \left(\frac{1}{1.52}\right)^2 \approx 1/3$), but the near-equatorial latitude of Gale crater results in an enhancement of the solar energy at the surface, which offsets that reduction. It is therefore plausible that, at least for certain configurations of obliquity and eccentricity, perennially ice-covered lakes similar to the ones observed at high-latitudes in Antarctica persisted in equatorial regions at Mars during the Hesperian.

Ice thickness calculation for Hesperian lakes

We compute the energy budget for a perennially ice-covered lake located inside Gale crater. For the sake of simplicity, we assume a regional forcing of the atmospheric temperatures above the lake, meaning that the

temperature at the surface of the lake is known and prescribed by the energy budget over the large, mostly dry area, that surrounds Gale crater (i.e. Eq. (15) and Figure 7). Since the ice cover sits on top of a liquid water column, the temperature at the bottom of the ice cover is also known and equal to 273K. Thus, with the top and bottom temperatures of the ice cover fully constrained, the energy balance can be used to derive the thickness of the ice cover. The ice thickness equation is adapted from McKay et al. (1985):

$$\bar{Z} = \frac{b \ln\left(\frac{T_o}{T_R}\right) + c(\bar{T}_R - T_o) - F_{sun}h\left(1 - e^{-\frac{\bar{Z}}{h}}\right)}{F_{geo} + \rho_{ice}\nu L(1 - \gamma_{glacier})} \quad (17)$$

with \bar{Z} the annual mean value for the ice-cover thickness, b , c defining the ice thermal conductivity (see Table 5 in the Appendix), $T_o=273\text{K}$ the temperature at the ice/liquid interface, \bar{T}_R the annually-averaged regional temperature, F_{sun} the effective solar energy available at the top of the ice cover, h the attenuation length of solar radiation within the ice, ρ_{ice} the ice density, ν the freezing rate at the bottom of the ice cover and equal to the sublimation rate in Eq. (1), L the latent heat of fusion for water, F_{geo} the geothermal flux and $\gamma_{glacier}$ a new term that represents the fraction of water input to the lake provided as melted ice from the glacier.

When $\gamma_{glacier}$ is set to zero, the lake is entirely resupplied by summer melt or subglacial flows, Eq. (17) is the same as in McKay et al. (1985), and the term $\rho_{ice}\nu L$ corresponds to the energy released at the bottom of the ice cover as the water freezes. When $\gamma_{glacier}$ equals one, no latent heat term appears in Eq. (17): latent heat is still released at the bottom of the ice cover when the water freezes, but an equal amount of energy was needed to first melt that same volume of ice from the glacier so the net contribution is zero. When $\gamma_{glacier}$ is different from 0 or 1, we must verify that the mass balance for the ice cover is still valid. Let ν_f be the freezing rate at the bottom of the ice cover, ν_{liquid} , the deposition rate for water brought into the lake by summer melt or subglacial flows and ν_{melted} the deposition rate for water brought into the lake by the ice melted from the glacier. Then, the total mass of water frozen at the bottom of the ice cover over one year is:

$$\begin{aligned} \underbrace{\rho_{ice}\nu_f A}_{\text{frozen bottom}} &= \underbrace{\rho_{ice}\nu_{liquid} A}_{\text{provided by melt streams}} + \underbrace{\rho_{ice}\nu_{melted} A}_{\text{provided by glacier}} \quad [kg/yr] \\ &= \rho_{ice}(1 - \gamma_{glacier})\nu A + \rho_{ice}\gamma_{glacier}\nu A \\ &= \rho_{ice}\nu A \end{aligned} \quad (18)$$

We have $\nu_f = \nu$ so ablation from the surface is still balanced by freezing at the bottom of the ice cover and mass is conserved. The energy released per unit area at the bottom of the ice cover when water freezes is $\rho_{ice}\nu_f L = \rho_{ice}\nu L$, the energy used to melt the glacier per unit area is $\rho_{ice}\nu_{melted} L = \rho\gamma_{glacier}\nu L$ and both terms appear in the denominator of Eq. (17). Following McKay (2004), we use a simplified two-band model to define the optical properties for the ice: albedo, transmissivity, are assumed to be uniform in the visible and ice is considered opaque to wavelengths larger than 700 nm. This approximation is justified by both measurements and theory (McKay et al., 1994; McKay, 2004; Bohren, 1983), and the effective solar energy available to melt the ice is:

$$F_{sun} = f_{700}(1 - a_{ice})Q_{sun\downarrow}^{sfc} \quad (19)$$

with f_{700} the fraction of solar energy for wavelengths below 700nm (photosynthetically active radiation or PAR) that penetrates the ice cover, a_{ice} the visible albedo over the ice, and $Q_{sun\downarrow}^{sfc}$ the solar flux at the surface from Eq. (16) and Figure 8. Note that since ice is mostly opaque to infrared radiation, we expect the ice cover thickness to decrease for atmospheres with strong greenhouse warming because of the higher ambient temperatures (i.e. lower conductive flux driving the freezing of the ice and higher ablation rates) and not directly because of the increased atmospheric infrared back radiation as the latter is not deposited at the bottom of the ice cover.

We show in the Appendix that the solution for the annual mean thickness \bar{Z} in Eq. (17) is:

$$\begin{cases} \bar{Z} = h \left(W \left(\frac{e^{\frac{\beta}{\alpha}}}{\alpha} \right) - \frac{\beta}{\alpha} \right) \\ \alpha = \frac{F_{geo} + \rho_{ice}\nu L(1 - \gamma_{glacier})}{F_{sun}} \\ \beta = 1 - \frac{b \ln\left(\frac{T_o}{T_R}\right) + c(\bar{T}_R - T_o)}{F_{sun}h} \end{cases} \quad (20)$$

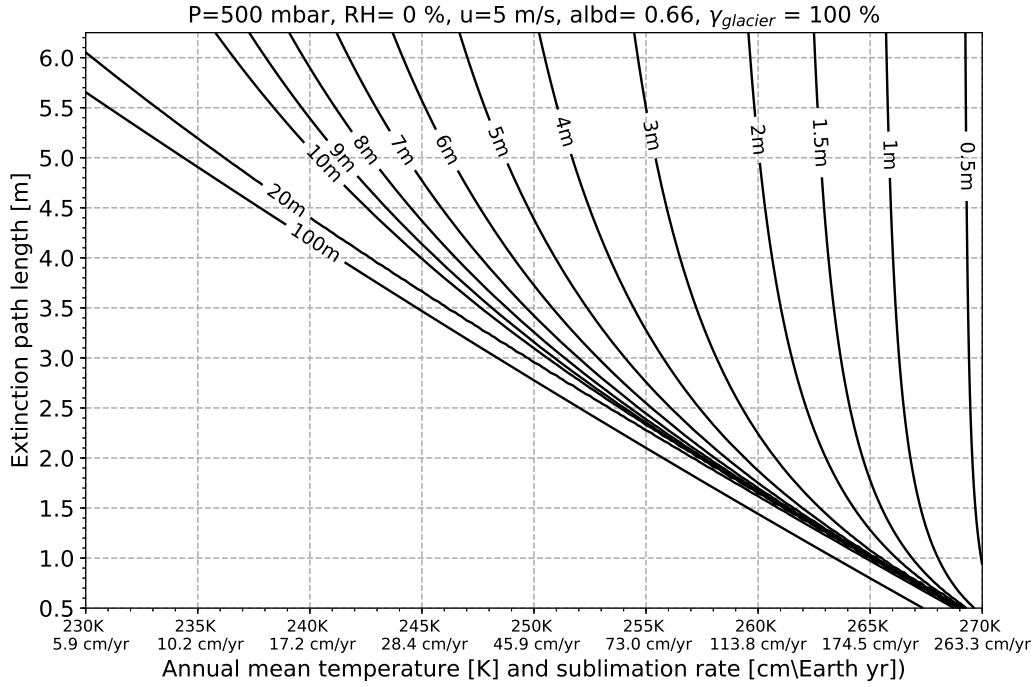


Figure 9: Ice thickness as a function of the extinction path length and mean annual surface temperature for a glacier-fed lake

with W the Lambert-W function. Using Eq. (20), the annual mean thickness \bar{Z} is computed for different combinations of ice extinction path lengths and mean annual surface temperatures. The mean equatorial surface temperatures \bar{T}_R range between 230K (weak greenhouse warming due to CO_2 only, see Figure 7) to 270K (up to +40K of warming due to some unspecified radiatively active species, e.g. a reducing H_2 or CH_4 atmosphere as in Wordsworth et al. (2017)). It is interesting to consider the specific case of clear ice in Antarctica as the ice has to be relatively transparent for this model to work. The 3 m thick ice cover on Lake Untersee has a visible albedo of 0.66 and a PAR transmissivity $T_{PAR} = (1 - a_{ice})e^{-\tau/h}$ of 0.05 (Andersen et al. (2011)), implying an extinction path length $h = 1.6$ m. On Lake Hoare, the average value of h is ~ 1 m for the entire ice cover, but for the lower layers of clear ice $h = 2.3$ m (an extinction coefficient of 0.435 m^{-1}) since attenuation near the surface of this ice cover is due primarily to accumulation of airborne dust. We consider extinction path lengths ranging from $h=0.5\text{m}$ to $h=6.25$ m for very clear ice (an extinction coefficient of 0.16 m^{-1} , see McKay et al. (1994)).

The thickness of the ice cover is shown in Figure 9 for a 500 mbar atmosphere, assuming surface winds of 5 m/s, an albedo of 0.66, a dry atmosphere (the relative humidity is $RH=0\%$), and for the limiting case where the lake is entirely resupplied by subaqueous melting of the glacier ($\gamma_{glacier}=1$). Figure 9 shows that for a mean annual temperature of 230K (weak greenhouse warming due to CO_2 only), there is no thin ice solution, that we define as the cases where the ice thickness is less than 10 meters. This is comparable to the range of values for the perennially ice-covered lakes in Antarctica, typically 3-6 m (McKay et al., 1985; Doran et al., 1994; Wand et al., 1997). However, when the ice is very clear ($h=5\text{m}$) thin ice solutions exist for annual mean temperatures as low as 240K, even though the maximum annual temperature never reaches 273K. At 255K, the requirement on the extinction path length for a 10 m thickness decreases to $h=2.4\text{m}$ and an ice cover thickness similar to Lake Untersee (3 m) is obtained for very clear ice ($h=5.5\text{m}$). To summarize, extinction path lengths $>2.4\text{m}$ are required in order to have a lake system resupplied entirely by subaqueous melting of a glacier for these very cold temperatures ($<240\text{K}-255\text{K}$). This requires the ice to be generally clearer than the ices for the lakes in Antarctica and also results in thicker ice covers (e.g. 10 m vs $\sim 3-6$ m for the Antarctic lakes). For clean ice covers such as Lake Untersee and the lower ice layers of Lake Hoare the main source of opacity is scattering due to the presence of bubbles trapped in the ice (McKay et al., 1994). These bubbles are formed due to the supersaturation of the lake water in gas (mostly nitrogen and oxygen Priscu et al. (1999); Andersen et al. (2011)). Therefore, the ice transparency for Hesperian perennially-covered lakes would have been intrinsically correlated with the saturation

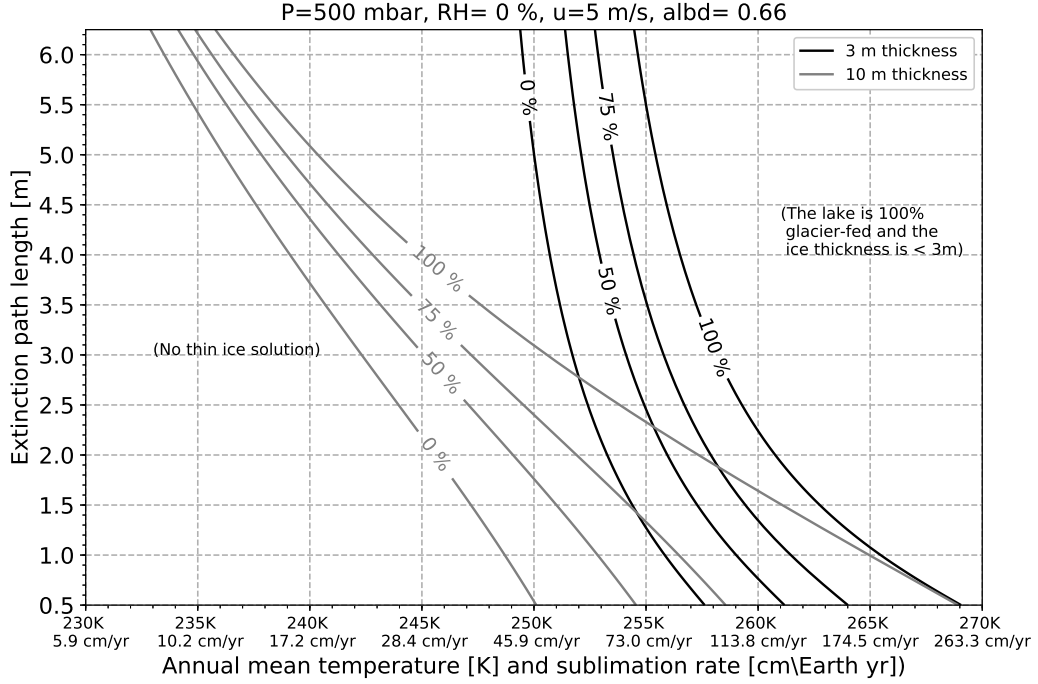


Figure 10: Percentage of the lake's water that can be resupplied by a glacier while keeping the ice cover thickness under 3 meters (black) and 10 meters (grey)

level for the lake's water, and extinction path lengths $h \gg 2.3$ m are plausible if the bubble content for the ice was low. Figure 9 is a limiting case because we assumed that the lake was entirely resupplied by subaqueous melting of the glacier. The existence of subglacial flows would allow to partially recharge the lake without ever contacting the atmosphere (no requirement for $T > 273$ K) while inducing no penalty on the energy balance in Eq. (17) since the water comes as liquid and does not require prior melting of the ice. Furthermore, we saw in Figure 7 that for even for moderate surface pressures ($P < 500$ mbar) the daily maximum temperature can reach the freezing point even though the mean annual temperatures stay as cold as 220 K. Therefore, it is reasonable to assume that even if the seasonal temperatures stayed below freezing, a fraction of the lake water could have been resupplied by daytime summer-melt, as it is the case in the Dry Valleys in Antarctica (McKay et al., 1985).

We will now consider intermediate scenarios where the lake is resupplied by both subaqueous melting of the glacier, subglacial flows and summer meltwater. For a given mean ice thickness, the fraction of water supplied by melting from the glacier γ_{glacier} in Eq. (17) is easily derived as a function of the ice cover properties (extinction path length, albedo), and the climatology (solar insolation, regional temperature \overline{T}_R , ablation rates v):

$$\gamma_{\text{glacier}} = 1 + \frac{F_{\text{geo}}}{\rho_{\text{ice}} v L} - \frac{b \ln\left(\frac{T_o}{T_R}\right) + c(\overline{T}_R - T_o) - F_{\text{sun}} h \left(1 - e^{-\frac{\overline{Z}}{h}}\right)}{\rho_{\text{ice}} v L \overline{Z}} \quad (21)$$

Eq. (21) shows the maximum amount of lake water that can be resupplied by subaqueous melting of the glacier given a set of extinction path length and surface temperature, and for two thicknesses of interest, $\overline{Z} = 3$ m and $\overline{Z} = 10$ m.

When only a $1/4$ of the lake water's is resupplied by summer melt or subglacial flows and for a conservative value for the extinction path length $h = 2$ m, the temperature requirement for thin (< 10 m) ice covers drops from $\overline{T}_R \sim 258$ K to $\overline{T}_R \sim 252$ K (grey 75% contour in Figure 10). Similarly, for that same extinction path length $h = 2$ m, ice covers as thin as 3 meters are possible at 253 K when all the water is provided as summer melt (black 0% contour in Figure 10).

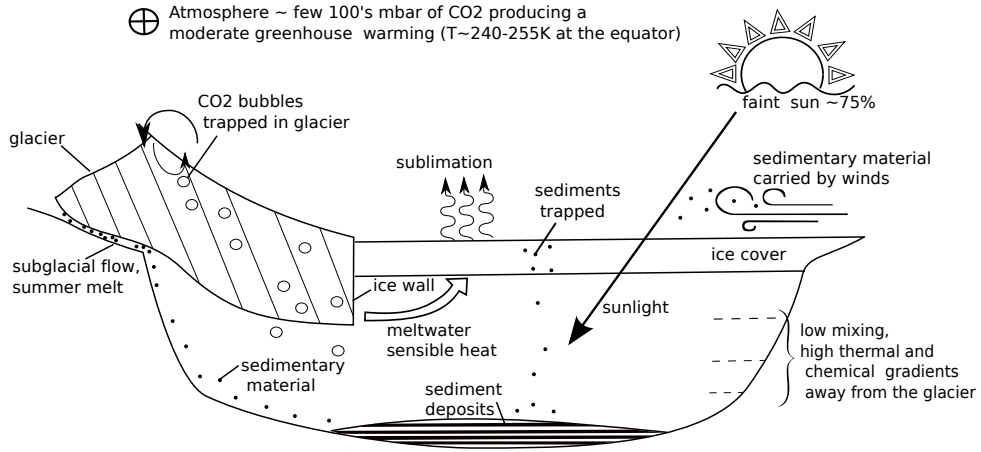


Figure 11: A cold hydrological system at Gale crater during the Hesperian

Providing that the ice is sufficiently clear (extinction path length $h > 2$ m), the ice-covered lake model can explain how a liquid environment could have been sustained at Gale crater through the Hesperian. In fact, the perennially ice-covered lakes could have subsisted as long as a source of meltwater (here a glacier) was available to resupply the lakes without the need for mean annual temperatures above freezing which no climate model has been able to reproduce. As a rough estimate, for the equatorial temperatures ~ 10 - 15 K above the global mean value (see Figure 6), mean annual temperatures at Gale crater $\overline{T}_R = 240$ - 255 K correspond to global mean temperatures $\overline{T}_G \sim 230$ - 245 K. The latest results from [Wordsworth et al. \(2017\)](#) suggest that this range of temperature is readily obtained with 0.5 - 1 bar of CO_2 and ~ 1 - 5% H_2 , with less or no reducing species at all if the surface pressure is greater than 1 bar.

Proposed geological context and implications for the carbonate content of the sediment

Based on these results, we propose the geological context illustrated in Figure 11 for Hesperian lakes with: a) an ice cover that limits the evaporation losses and seals the lake from the atmosphere b) a glacial wall, subglacial flows or episodic melt streams which resupply the lake with meltwater, c) sediment material being transported through the ice cover from the base of the glacier.

The MSL mission discovered that the carbonate content of the sediment is low, typically below the detection limit of the CheMin instrument of ~ 1 wt% ([Ming et al., 2014](#)). The nondetection of carbonate in the sediment in Gale crater is an unexpected outcome in the context of sediment formed in open water lakes that are in thermodynamic equilibrium with a CO_2 atmosphere, since sustaining unfrozen lakes requires a substantial amount of CO_2 to provide enough greenhouse warming ([Bristow et al. \(2017\)](#)) and note that groundwater infiltration was proposed as a plausible mechanism to produce magnetite and H_2 in high p_{CO_2} atmospheres [Tosca et al. \(2018\)](#)) On Earth, perennially ice-covered lakes are not necessarily in equilibrium with the atmosphere. For instance Lake Untersee is supersaturated in nitrogen, oxygen, and, interestingly, deficient in CO_2 ([Wand et al., 1997](#)). This is due to its perennial ice cover which isolates (seals) the lake from the environment, and to the presence of microbial communities that consume the CO_2 dissolved in the water ([Townsend et al., 2009](#); [Andersen et al., 2011](#)). In our model the sublimation of the ice cover is balanced by melting of the glacier, so any CO_2 trapped within the glacier will eventually be dissolved in the water.

The carbon flux entering the lake and available for carbonate precipitation is therefore still related to the atmospheric pressure, however it is now controlled by both the sublimation of the ice cover and the CO_2 bubble content of the glacier. With carbon itself making about 27% of the mass of a CO_2 molecule, the carbon flux going into the lake is can be estimated as:

$$F_C = 0.27 F_{ice} V_{bubble} \rho_{\text{CO}_2} \quad [\text{kg}_C/\text{m}^2/\text{yr}] \quad (22)$$

with F_{ice} in $[\text{kg}_{ice}/\text{m}^2/\text{yr}]$ the mass flux of ice from the glacier melting into the lake and distributed over the surface area of the lake, $(V_{bubble} \rho_{\text{CO}_2})$ the mass of CO_2 trapped in one kg of ice with V_{bubble} the bubble content of the glacier in $[\text{m}^3/\text{kg}_{ice}]$ and ρ_{CO_2} in $[\text{kg}_{\text{CO}_2}/\text{m}^3_{ice}]$ the density of CO_2 bubbles. Furthermore, the density ρ_{CO_2} is related to the atmospheric pressure P_{CO_2} :

$$\rho_{CO_2} = \frac{P_{CO_2} M_{CO_2}}{RT} \quad (23)$$

with $M_{CO_2} = 0.044$ [kg/mol] the molecular mass of CO_2 , $R = 8.314$ [J/kg/mol] the gas constant and T the air temperature. Note that in the case where the lake is entirely resupplied by subaqueous melting of a glacier, the ice mass flux from the glacier F_{ice} exactly balances the sublimation rate of the ice cover $E_{combined}$ from Eq. (1), written in units of [kg_{ice}/m²/yr]. For instance, with $F_{ice} = 600$ [kg/m²/yr] (ablation rate of 60 cm per Earth year, see Figure 3), a relatively low value for the surface pressure $P_{CO_2} = 50$ mbar, $T = 255$ K, and a typical bubble content for Antarctic glaciers $V_{bubble} = 10^{-4}$ [m³/kg_{ice}] (Craig et al., 1993), we found a carbon flux entering the lake equal to $F_C \sim 1.6$ g/yr/m². We adapted Bristow et al. (2017) calculations to account for the reduced input of carbon into the water with respect to open water lakes and estimate a new calcite content for the sediment. Assuming that all the carbon ends up as calcite in the sediment so that the area of sediment matches the area of ice cover, a sediment density of 3 g/cm³, a porosity of 0.6, a carbon flux of 1.6 g/yr/m², and a sedimentation rate through the ice cover of 0.1 cm yr⁻¹, we found that the calcite makes ~ 1 wt% of the sediment, which is consistent with the detection limit of CheMin. Since the carbon flux F_C scales linearly with the atmospheric pressure and the bubble content, higher surface pressures require bubble contents lower than those typically found in the Antarctic glaciers in order to stay below the 1 wt.% limit (e.g. $V_{bubble} \leq 10^{-5}$ [m³/kg_{ice}] for $P_{CO_2} = 500$ mbar). Furthermore, if the CO_2 carried into the lake in these glacier bubbles is largely converted to carbonate then there would be less buildup of dissolved gases in the water column. This would reduce the bubble formation in the ice cover and imply clear ice, which is favorable to the formation of a thin ice cover.

Perennially ice-covered lakes also allow for stratification in water temperature and chemistry as ice covers prevent wind-driven turbulence within the lakes (Obryk et al., 2016; Townsend et al., 2009; Priscu et al., 1999). Lake Untersee is damned by a glacier so cooling of the water near the glacial wall induces a buoyancy-driven circulation that mixes the lake where the glacier reaches (Steel et al., 2015; Faucher et al., 2019). However, part of the lake is shielded from these currents and remains stratified (Bevington et al., 2018). It is worthwhile to reconsider the nature of the lake deposits observed in Gale crater in the context of an ice-covered lake. We hypothesize that the intrinsic physical stability of a perennially ice-covered lake would be generally consistent with the chemical stratification observed within the sediment in Gale crater (Hurowitz et al., 2017).

Finally, we would like to comment on the potential of perennially ice-covered lakes as habitats for biology. In Antarctica, microbial communities sometimes produce thick mats at the lake bottom of perennially ice-covered lakes, including Lake Untersee (Andersen et al., 2011; Hawes et al., 2013; Mackey et al., 2015; Sumner et al., 2016). Likewise, if microbial communities were present on early Mars, perennially ice-covered lakes might have provided a stable, long-lived shelter for their persistence and it is plausible that cosmic rays would have mostly erased their traces from the shallow Martian subsurface (Pavlov et al., 2012; Montgomery et al., 2016). Nevertheless, if perennially ice-covered lakes did exist on Mars, sites like Gale crater may be ideal places to search for biosignatures, a few meters beneath the surface.

5. Summary and caveats for the ice-covered lake hypothesis

The ice-covered lake model provides an interesting way to decouple the mineralogy and the climate by limiting the gas exchanges between the sediment and the CO_2 atmosphere, and it eliminates the requirement for annual mean temperatures above the freezing point. We foresee that moderate surface pressures (< 1 bar of CO_2) would still result in a low calcite content within the sediment while allowing for enough greenhouse warming ($T_R \sim 240$ K–255 K) to prevent the lakes from freezing to the bedrock. In Gale crater, it is primarily the presence of well cemented and laterally extensive laminated mudstones that suggests a lacustrine environment (Grotzinger et al., 2014, 2015). On Earth, laminated mud may be deposited from inflowing streams but also by abutting glaciers in perennially-covered lakes, as is the case for Lake Untersee (Andersen et al., 2011; Levitan et al., 2011; Rivera-Hernandez et al., 2019). However, contrary to what had been observed in the sediment deposits at Gale crater, the laminated mud at Lake Untersee also contains disseminated medium sand to granule size sediment, with rare fine to medium gravel (Rivera-Hernandez et al., 2019). At Lake Untersee, the sand at the bottom of the lake originates from the ice cover: the lake ice acts as a trap for aeolian sediment and the sand then penetrates the ice cover either by melting the ice or migrating downward through conduits such as ice-grain boundaries, ice cracks, or gas bubble channels (e.g. M. Jepsen et al. (2010) and references therein). If the sand on a perennially ice-covered lake at Gale crater did not migrate through the ice (either due to the absence of conduits in the ice cover or the impossibility of melting

its way through the ice), this would result in the deposition of laminated mud from an abutting glacier without disseminated sand from the ice cover.

Admittedly, the Lake Untersee model may not explain all of the lake deposits in Gale crater, in particular, those that are interpreted to have a fluvial origin and require running water (Williams et al., 2013; Grotzinger et al., 2014, 2015; Anderson et al., 2015; Edgar et al., 2018). We saw in Figure 7 that peak daytime temperatures reach 273K for pure CO₂ atmospheres with moderate surface pressures ($P < 500$ mbar) but this study has focused mostly on the steady-state climates and we did not address specifically the erosion potential of episodic snowmelt (see Kite et al. (2013)). Ephemeral streams and rivers form in the cold and hyperarid McMurdo Dry Valleys and induce erosion, deposition and the formation of alluvial fans and deltas (Head and Marchant, 2014; Shaw and Healy, 1980). Notably, the seasonal flow patterns for rivers in the Dry Valleys show a strong diurnal cycle associated with warmer daytime temperatures (Shaw and Healy, 1980). This make them compelling analogues for Gale crater, as equatorial regions on Mars typically experience strong seasonal temperature cycles (due to obliquity and eccentricity effects), and large (tens of kelvin) diurnal temperature cycles. Gale crater also contains a handful of geologic landforms that have been interpreted as possible evidence for past cold-climate environments such as decametric polygons (Oehler et al., 2016), and lobate features (FairĀ'n et al., 2014).

Conversely, the lack of unambiguous evidence for a cold climate at Gale crater has been pointed out: frost wedges, glacial tills, and glaciogenic sedimentary deposits (e.g. coarse cobbles, boulder conglomerates) are typically absent from MSL's observations (Grotzinger et al., 2015), which is a weakness for the Lake Untersee model. If a cold-based glacier was present in Gale crater, it is plausible that its presence in the rock record would be subtle if sliding did not occur at the rock-ice interface. On Earth cold-based glaciers have low erosion potential (compared to temperate glaciers) and can sometimes preserve the landscape rather than erode bedrock (Marchant and Head, 2007; Richardson and Holmlund, 1996). Similarly, one can hypothesize that freeze-thaw weathering would be fairly limited in a cold environment that experiences only episodic melting rather than regular freezing/melting cycles. Rather than refuting the picture of open water lakes that has emerged from detailed sedimentological observations by the MSL science team, we support FairĀ'n et al. (2014) who raised a fundamental question: how much of the stratigraphy observed at Gale crater could possibly be interpreted with a cold hydrological cycle?

6. Appendix

A. Derivation of the free evaporation

The evaporation resulting from free convection is (Ingersoll (1971); Adams et al. (1990); Dundas and Byrne (2010)):

$$E_{free} = \frac{1}{\rho_{ice}} K_M \frac{M_{H_2O}}{R} \left(\frac{e_{sat}^{surf}}{T_{surf}} - RH \frac{e_{sat}^{atm}}{T_{atm}} \right) \quad [m/s] \quad (24)$$

Introducing $D = D_{H_2O/CO_2} [m^2 \cdot s^{-1}]$ the diffusion coefficient of water vapor into the CO₂ atmosphere and $\nu [m^2 \cdot s^{-1}]$ the kinematic viscosity evaluated at $\frac{1}{2}(T_{surf} + T_{atm})$, Adams et al. (1990) defined the bulk coefficient K_M as:

$$K_M = 0.14 \left(\frac{D^2 B}{\nu} \right)^{\frac{1}{3}} \quad [ms^{-1}] \quad (25)$$

with B the buoyancy force per unit mass resulting from the presence of H₂O in the denser CO₂ atmosphere:

$$B = g \frac{\rho_{atm} - \rho_{surf}}{\rho_{surf}} \quad [ms^{-2}] \quad (26)$$

with ρ_{atm} and ρ_{surf} the atmospheric densities of the CO₂ /H₂O mixture of the ambient air and at the surface, respectively. We have:

$$\begin{aligned} \frac{\rho_{atm} - \rho_{surf}}{\rho_{surf}} &= \left(\left(\frac{P_{CO_2}^{atm} M_{CO_2}}{RT_{atm}} + \frac{e_{atm}^{atm} M_{H_2O}}{RT_{atm}} \right) \right. \\ &\quad \left. - \left(\frac{P_{CO_2}^{surf} M_{CO_2}}{RT_{surf}} + \frac{e_{sat}^{surf} M_{H_2O}}{RT_{surf}} \right) \right) \\ &\quad \times \frac{1}{\frac{P_{CO_2}^{surf} M_{CO_2}}{RT_{surf}} + \frac{e_{sat}^{surf} M_{H_2O}}{RT_{surf}}} \end{aligned} \quad (27)$$

with P_{atm} the total pressure, and P_{CO_2} the partial pressure of CO_2 . Replacing $P_{CO_2} = P_{atm} - e$ respectively at the surface and in the atmosphere and rearranging (27) we found:

$$\begin{aligned} \frac{\rho_{atm} - \rho_{surf}}{\rho_{surf}} &= \left(M_{CO_2} P_{atm} \left(\frac{T_{surf}}{T_{atm}} - 1 \right) \right. \\ &\quad - \frac{T_{surf}}{T_{atm}} (M_{CO_2} - M_{H_2O}) e^{atm} \\ &\quad \left. + (M_{CO_2} - M_{H_2O}) e_{sat}^{surf} \right) \\ &\quad \times \frac{1}{M_{CO_2} P_{atm} - (M_{CO_2} - M_{H_2O}) e_{sat}^{surf}} \end{aligned} \quad (28)$$

Using $e^{atm} = RH e_{sat}^{atm}$, we obtain:

$$\begin{aligned} \frac{\rho_{atm} - \rho_{surf}}{\rho_{surf}} &= \left(M_{CO_2} P_{atm} \left(\frac{T_{surf}}{T_{atm}} - 1 \right) \right. \\ &\quad \left. + (M_{CO_2} - M_{H_2O}) \left(e_{sat}^{surf} - \frac{T_{surf}}{T_{atm}} RH e_{sat}^{atm} \right) \right) \\ &\quad \times \frac{1}{M_{CO_2} P_{atm} - (M_{CO_2} - M_{H_2O}) e_{sat}^{surf}} \end{aligned} \quad (29)$$

Assuming $T_{atm} \sim T_{surf}$, we have:

$$\frac{\rho_{atm} - \rho_{surf}}{\rho_{surf}} = \frac{(M_{CO_2} - M_{H_2O}) e_{sat}^{surf} (1 - RH)}{M_{CO_2} P_{atm} - (M_{CO_2} - M_{H_2O}) e_{sat}^{surf}} \quad (30)$$

and we combine Eq. (24), (25) and (30) and find:

$$E_{free} = \frac{1}{\rho_{ice}} \underbrace{0.14 D \left(\frac{g \frac{\rho_{atm} - \rho_{surf}}{\rho_{surf}}}{v^2} \left(\frac{v}{D} \right) \right)^{\frac{1}{3}}}_{K_M} \frac{M_{H_2O}}{RT_{surf}} e_{sat} (1 - RH) \quad [m \cdot s^{-1}] \quad (31)$$

We used the formulations provided in Altheide et al. (2009) for $D_{H_2O/CO_2}(T, P)$, $e_{sat}(T)$, $v(T, P)$ to obtain a formulation for the free evaporation rate as a function of the surface pressure, surface temperature and relative humidity. Note that Eq. (31) is similar to the expression from Altheide et al. (2009) when $RH = 0$, or Ingersoll (1971) who assumed $\frac{v}{D} \sim 1$, $RH = 0$, $\Delta\eta = \frac{\rho_{sat}}{\rho_{ice}}$ and 0.17 close to 0.14.

Note that at high relative humidity, the evaporation rate decreases for two reasons. First the buoyancy B decreases as the relative difference in density $\frac{\rho_{atm} - \rho_{surf}}{\rho_{surf}}$ between the ambient air and the surface decreases (physically, this is due to the difference in molar masses between the denser CO_2 and the lighter H_2O since a mixture of $CO_2 + H_2O$ is lighter than CO_2 alone). Second, the difference between the saturated vapor density in the ambient air and at the surface:

$$\frac{M_{H_2O}}{R} \left(\frac{e_{sat}^{surf}}{T_{surf}} - RH \frac{e_{sat}^{atm}}{T_{atm}} \right) \quad (32)$$

decreases. Eventually, when the air is saturated ($RH = 100\%$) the evaporation shuts off completely.

On the other hand, when the surface temperature is warmer than the ambient air $T_{atm} < sim T_{surf}$, an additional buoyancy force remains in Eq. (29) and leads to higher evaporation rates.

B. Derivation of the wind-driven evaporation

We have (Adams et al., 1990; Dundas and Byrne, 2010):

$$E_{forced} = \rho_{atm} \frac{Ku^*}{\ln\left(\frac{z_s}{z_0}\right)} (q_{sat} - q_{atm}) \quad [kg/s] \quad (33)$$

with ρ_{atm} the atmospheric density, $\kappa \sim 0.4 \text{ m s}^{-1}$ the Von Karman constant, u^* a friction velocity and $q = \frac{M_{H_2O}}{M_{CO_2}} \frac{e}{P_{atm}}$ the specific humidity. Assuming a log-wind profile for the boundary layer:

$$u = \frac{u^*}{\kappa} \left[\ln \left(\frac{z5}{z0} \right) + \phi \right] \quad [m/s] \quad (34)$$

with $\phi \sim 0$ for a neutral boundary layer, combining (33) and (34), we obtain:

$$E_{forced} = \frac{1}{\rho_{ice}} A \frac{M_{H_2O}}{R} \left(\frac{e_{sat}^{surf}}{T_{surf}} - RH \frac{e_{sat}^{atm}}{T_{atm}} \right) \quad [m/s] \quad (35)$$

and

$$A = \frac{\kappa^2}{\ln \left(\frac{z5}{z0} \right)^2} \quad [m/s] \quad (36)$$

with M_{H_2O} the molecular weight of water, $R=8.314 \text{ [J/kg/mol]}$ the gas constant, $\kappa = 0.4$ the Von Karman's constant, u the wind speed at a reference altitude above ground, T_{atm} and T_{surf} the air and surface temperatures, e_{sat} and $e = RHe_{sat}$ the saturated and ambient vapor pressure of the air. We used the surface roughness $z0=0.01\text{m}$, and $z5=5\text{m}$ as a reference altitude.

C. Derivation of the analytical solution for the energy balance model

North (1975b) gives a particular solution to Eq. (9), for the OLR :

$$OLR = \sum_{n,even} \frac{Q H_n(x_s) p_n(x)}{n(n+1)D' + 1} \quad (37)$$

where Q is a globally-averaged value for the solar flux ($Q = \frac{\varphi_0}{4}$ in our study), x the sine of the latitude with x_s the position of the discontinuity in albedo at the edge of an ice sheet (if any), $D' = \frac{D}{B}$ in our study, H_n the insolation components and p_n the Legendre polynomials. For Earth's present-day obliquity (and by analogy for Mars' present-day obliquity as $\beta_E = 23^\circ \sim \beta_M = 25^\circ$), North (1975b) shows that expending Eq. (37) to the first two terms is generally sufficient. In order to solve Eq. (9) for a wide range of obliquities, we use the fourth degree approximation from Nadeau and McGehee (2017) for the mean annual insolation as a function of the latitude:

$$\begin{cases} \overline{Q_{sun}}(x) = \frac{\varphi_0}{4 \sqrt{1-e^2}} (1 + S_2 p_2(x) + S_4 p_4(x)) \\ S_2 = -\frac{5}{8} p_2(\cos(\beta)) \\ S_4 = -\frac{9}{64} p_4(\cos(\beta)) \end{cases} \quad (38)$$

with φ_0 the solar constant, e the eccentricity, β the obliquity and p_n the Legendre polynomials:

$$\begin{cases} p_0(x) = 1 \\ p_2(x) = (3x^2 - 1)/2 \\ p_4(x) = (35x^4 - 30x^2 + 3)/8 \\ p_6(x) = (231x^2 - 315x^4 + 105x^2 - 5)/16 \\ p_8(x) = (6435x^8 - 12012x^6 + 6930x^4 - 1260x^2 + 35)/128 \end{cases} \quad (39)$$

The planetary albedo, formally defined as the ratio of the reflected to upcoming shortwave radiations at the top of the atmosphere $a = \frac{Q_{sun}^{TOA}}{Q_{sun}^{TOA}}$, can vary due to several factors: a) the reflectance of the soil (presence of CO_2 ice), b) the optical properties of the atmosphere (increased scattering at higher pressures, presence of CO_2 clouds), and c) the difference in the solar zenith angle at different latitudes (obliquity-dependent).

Therefore, it is desirable to use a formulation for the annually-averaged co-albedo $\bar{a}(x) = (1 - \bar{a}(x))$ (i.e $\alpha_0 = 1 - a_0$, $\alpha_2 = -a_2$, $\alpha_4 = -a_4$) that will be appropriate for different climate scenarios. In place of the simple step function in North (1975a) or the discontinuous second order approximation in North (1975b), we use instead a continuous, fourth degree approximation for the co-albedo:

$$\bar{a}(x) = \alpha_0 + \alpha_2 p_2(x) + \alpha_4 p_4(x) \quad (40)$$

where the α_n coefficients can be, by order of increasing complexity for the parameterization:

- reduced to a global mean value α_0 (i.e. $\alpha_2 = \alpha_4 = 0$). α_0 is retrieved from the radiative transfer calculations for different surface pressures (the albedo increases with increasing pressure due to scattering) and averaged over all zenith angles
- approximated as a combination of a pressure-dependent term α_0 and the distribution of the incident shortwave radiation which is related to the annually-averaged value for the solar zenith angle:

$$\bar{\alpha}(x) = \alpha_0 + f_{co} (S_2 p_2(x) + S_4 p_4(x)) \quad (41)$$

with $\alpha_2 = f_{co} \times S_2$, $\alpha_4 = f_{co} S_4$, and f_{co} a fitting factor for the co-albedo with $f_{co} = -f_a$ and f_a the optional albedo factor from Table 3

- directly fitted to observations or modeling results from a Mars Global Climate Model (MGCM) where the polar caps are resolved and the dependence of the albedo on the solar zenith angle is explicitly computed.

Using equations (38-40), we can show that:

$$\left\{ \begin{array}{l} \bar{\alpha}(x) \overline{Q_{sun}}(x) = \frac{\varphi_0}{4 \sqrt{1-e^2}} \sum_{n=0,even}^{n=8} S a_n p_n(x) \\ S_{a0} = \frac{1}{5} S_2 \alpha_2 + \frac{1}{9} S_4 \alpha_4 + \alpha_0 \\ S_{a2} = S_2 \alpha_0 + \frac{2}{7} S_2 \alpha_2 + \frac{2}{7} S_2 \alpha_4 + \frac{2}{7} S_4 \alpha_2 + \frac{100}{693} S_4 \alpha_4 + \alpha_2 \\ S_{a4} = \frac{18}{35} S_2 \alpha_2 + \frac{20}{77} S_2 \alpha_4 + S_4 \alpha_0 + \frac{20}{77} S_4 \alpha_2 + \frac{162}{1001} S_4 \alpha_4 + \alpha_4 \\ S_{a6} = \frac{5}{11} S_2 \alpha_4 + \frac{5}{11} S_4 \alpha_2 + \frac{20}{99} S_4 \alpha_4 \\ S_{a8} = \frac{490}{1287} S_4 \alpha_4 \end{array} \right. \quad (42)$$

where S_n are the solar terms, α_n are the co-albedo terms, and p_n the Legendre polynomials. The higher order terms can be neglected ($S_{a8} = S_{a6} \sim 0$), and we obtained an expression for the annually-averaged solar radiation absorbed by an atmospheric column:

$$\bar{\alpha}(x) \overline{Q_{sun}}(x) = \frac{\varphi_0}{4 \sqrt{1-e^2}} (S_{a0} + S_{a2} p_2(x) + S_{a4} p_4(x)) \quad (43)$$

with $\varphi_0, \beta, e, S_{a0}, S_{a2}, S_{a4}$ dependent on the climate scenarios considered for early Mars (e.g. high obliquity, high eccentricity, presence of ice, reduced solar luminosity φ_0).

The formulation in Eq. (43) for the absorbed shortwave radiation is a continuous function of the latitude, which is a special case in North (1975b) (ice-free case, $x_s=1$). It follows that $H_n(1) = S a_n$, and using $T = \frac{OLR-A}{B}$ in Eq. (37) we can finally write the solution of the energy balance differential equation as:

$$\overline{T}_s(x) = \frac{\varphi_0}{4 \sqrt{1-e^2}} \sum_{n=0,even}^4 \frac{S a_n p_n(x)}{n(n+1)D+B} - \frac{A}{B} \quad (44)$$

D. Terms used in the time-dependent surface energy balance model

Downward shortwave radiation

The downward shortwave radiation $Q_{sun\downarrow}^{TOA}$ is derived from Levine et al. (1977); Allison and McEwen (2000).

$$\left\{ \begin{array}{l} Q_{sun\downarrow}^{TOA} = Q_{sun}^{mean} C_{Ls} C_{lat} \\ Q_{sun}^{mean} = 0.75 \frac{1370}{1.52^2} \\ C_{Ls} = \left(\frac{1 + e \cos(L_s - L_s^p)}{1 - e^2} \right)^2 \\ C_{lat} = \left(\sin(\phi) \sin(\delta) + \cos(\phi) \cos(\delta) \cos\left(\frac{2\pi t_{noon}}{T_{Mars}}\right) \right) \end{array} \right. \quad (45)$$

Q_{sun}^{mean} is the mean solar flux at Mars ~ 3.6 Gya fixed to 75% of today's value with 1370 Wm^{-2} the solar constant and 1.52 the distance to the Sun in astronomical units, C_{Ls} is a correction factor for the variations of the Sun-Mars distance with the solar longitude L_s , e is the eccentricity, $L_s^p = 248$ the solar longitude at perihelion. C_{lat} accounts for the solar zenith angle with ϕ the latitude, δ the solar declination with $\sin(\delta) = \sin(\beta) \sin(L_s)$ with β Mars' obliquity, t_{noon} the time elapsed after solar noon and $T_{Mars} = 88775s$ the length of a Martian solar day. See Levine et al. (1977) for the integration of the incident solar irradiance over a day including atmospheric attenuation.

Pressure [mbar]	D [$W/m^2/K$]	$Q_{IR\uparrow}^{TOA}(T) = A + B T$		$Q_{IR\downarrow}^{sfc} = A_1 + B_1 T$		Albedo	
		A	B	A_1	B_1	a_0	f_a
7	0.02	-212	1.54	-176	0.96	(see text)	
50	0.08	-274	1.78	-255	1.42	0.21	-0.033
100	0.14	-248	1.63	-286	1.61	0.23	-0.051
200	0.25	-208	1.40	-300	1.75	0.25	-0.075
500	0.46	-134	0.99	-341	2.04	0.29	-0.111
800	0.61	-93	0.77	-350	2.13	0.32	-0.128
1000	0.70	-72	0.66	-355	2.17	0.33	-0.135
1500	0.86	-40	0.49	-351	2.20	0.37	-0.143
2000	1.00	-19	0.39	-335	2.15	0.39	-0.146
2500	1.11	-6	0.32	-327	2.13	0.41	-0.146
3000	1.20	5	0.27	-318	2.10	0.43	-0.144
3500	1.28	13	0.23	-310	2.08	0.45	-0.142
4000	1.36	19	0.20	-303	2.06	0.46	-0.139
5000	1.49	30	0.15	-289	2.02	0.49	-0.134

Table 3: Estimates for the outgoing longwave radiation at the top of the atmosphere, downward infrared flux at the surface, and planetary albedo as a function of the surface pressure derived from the *fictive* temperature profiles (clear sky, no clouds, see Figure 5). The coefficients of determination R^2 for the linear fits to the OLR $Q_{IR\uparrow}^{TOA}$ and to the downward infrared flux at the surface $Q_{IR\downarrow}^{sfc}$ are greater than 0.95 and 0.88, respectively. For the planetary albedo (total reflection by atmosphere and the surface), we assume a surface albedo of 0.2. The global mean value for the co-albedo α_0 and fitting factor f_{co} are easily related to the global mean albedo a_0 and the optional albedo factor f_a using $\alpha_0 = 1 - a_0$ and $f_{co} = -f_a$. Estimates for the diffusivity D from Eq. (10) are also given in the table.

Downward longwave radiation at the surface

A rough estimate for the annually-averaged downward infrared radiation at the surface is also obtained from the radiative transfer calculations and available in Table 3. As for the OLR, we use a simple linear fit to the radiative transfer output:

$$\overline{Q_{IR\downarrow}^{sfc}} = A_1 + B_1 \overline{T_R} \quad (46)$$

with $\overline{T_R}$ the annually-averaged regional temperature obtained from Eq. (12).

Geothermal flux

The geothermal flux Q_{geo} is used as an energy input at the base of the model. We assumed a value $Q_{geo}=30$ mW/m^{-2} following Dundas and Byrne (2010). Note that this energy input is small relatively to the downward shortwave and longwave fluxes ($Q_{geo} \ll Q_{IR\downarrow}, Q_{sun}$).

Atmospheric temperature and sensible heat

For the atmospheric temperature, we use the parametrization from Dundas and Byrne (2010):

$$T_{atm} = T_{min}^b \cdot T_{surf}^{1-b} \quad (47)$$

with T_{min} the most recent diurnal minimum of the surface temperature, T_{surf} the current surface temperature and b an atmospheric parameter.

For the sensible heat, we use the formulation from Dundas and Byrne (2010); Williams et al. (2008):

$$\begin{cases} SH|_{free} = 0.14(T_{atm} - T_{sfc})k_{atm} \left(\frac{C_P \rho_{atm} g \frac{\rho_{atm} - \rho_{surf}}{\rho_{surf}}}{k_{atm} \nu} \right)^{\frac{1}{3}} \\ SH|_{forced} = \rho_{atm} C_P A u (T_{atm} - T_{surf}) \end{cases} \quad (48)$$

with k_{atm} the atmospheric thermal conductivity, C_P the specific heat, ν the kinematic viscosity, g the gravity, A the wind function from Eq. (36), and u the wind speed. Though the sensible heat losses are small with respect to the radiative losses for present-day surface pressure ($SH \sim 2.5-11$ $W/m^2 \ll \epsilon\sigma T^4$, see Schubert and Mitchell (2013)), they increase proportionally with the atmospheric density ρ_{atm} so the atmospheric temperature T_{atm} must be carefully related to T_{surf} in order to avoid an overestimation of the convective losses at high surface pressure.

For present-day Mars and for the early Mars cases with low surface pressure ($P \leq 100$ mbar), we used $b=0.2$ as in Dundas and Byrne (2010). For the present-day test case, using $b=0.2$ produced a noontime temperature

difference $T_{surf} - T_{atm} \sim 24\text{K}$, which is similar to the difference between the ground temperature and the mast air temperature $\sim 20\text{K}$ measured by MSL in Gale crater (Martínez et al. (2017)). For the high surface pressure cases ($P \geq 500$ mbar), b was tuned to 0.1 to account for the increased efficiency of the upward heat transport by turbulent eddies which tend to homogenize the air temperatures near the surface ($T_{surf} - T_{atm}$ decreases). The choice $b=0.1$ produces sensible heat fluxes at $P=1$ bar which are similar to Earth's convective losses: 24-83 W/m^2 in average, with peak afternoon values not exceeding 250 – 300 W/m^2 (Schubert and Mitchell, 2013; Wang and Bras, 2001).

Conductive flux

The conductive flux is $Q_{cond} = k \frac{\partial T}{\partial Z}$ with k the thermal conductivity of regolith, T the temperature and Z the depth was solved using an implicit finite difference scheme with Von Neumann boundary conditions at the top and bottom of the domain.

Table of coefficients used for the time-marching surface energy balance

Parameter	Value
Thermal conductivity k	0.065 $\text{Wm}^{-1}\text{K}^{-1}$
Density regolith ρ_{rego}	1500 kg.m^{-3}
Spe. heat capacity regolith $c_{p,rego}$	750 $\text{J.kg}^{-1}\text{K}^{-1}$
Molar mass CO_2 M_{CO_2}	44 g.mol^{-1}
Spe. heat capacity CO_2 c_{p,CO_2}	770 $\text{J.kg}^{-1}\text{K}^{-1}$
Thermal conductivity CO_2 k_{atm}	0.02 $\text{Wm}^{-1}\text{K}^{-1}$
Wind u	5 ms^{-1}
albedo a	Varies as in Table 3
Atm. parameter b	0.1-0.2
emissivity ϵ	1
obliquity θ	25°
geothermal flux F_{geo}	0.03 Wm^{-2}

Table 4: Simulation parameters and physical constants for Martian regolith. The values are close to the ones used in the Ames-GCM and consistent with Grott et al. (2007);Stoker et al. (1993); Zent et al. (2009)

E. Coefficients used for the ice thickness calculation

Parameter	Value	Comment
Thermal conductivity k_{ice}	780/T+0.615 W/m/K	(McKay et al., 1985)
Density ice ρ_{ice}	900 kg.m^{-3}	Assume pure ice
Latent heat L	334000 J/kg	
Wind u	5 ms^{-1}	Same as Eq. (15)
Relative humidity RH	0%	hyper-arid climate
Geothermal flux F_{geo}	0.03 Wm^{-2}	Same as Eq. (15)
Albedo a_{ice}	0.66	Same as Lake Untertsee (McKay, private comm.)
% of energy <700 nm f_{700}	50%	(McKay, 2004)

Table 5: Simulation parameters for the ice thickness calculation and physical constants for the ice

F. Analytical solution for the ice cover thickness

Eq. (17) is a non-linear equation in \bar{Z} . We re-organize it and define the constants α and β as follows:

$$\begin{aligned}
\bar{Z} &= \frac{b \ln\left(\frac{T_o}{T_R}\right) + c(\bar{T}_R - T_o) - F_{sun}h \left(1 - e^{-\frac{\bar{Z}}{h}}\right)}{F_{geo} + \rho_{ice}vL(1 - \gamma_{glacier})} \\
\Rightarrow \bar{Z} \left(F_{geo} + \rho_{ice}vL(1 - \gamma_{glacier})\right) &= b \ln\left(\frac{T_o}{T_R}\right) + c(\bar{T}_R - T_o) \\
&\quad - F_{sun}h + F_{sun}he^{-\frac{\bar{Z}}{h}} \\
\Rightarrow \bar{Z} \left(F_{geo} + \rho_{ice}vL(1 - \gamma_{glacier})\right) & \\
+ F_{sun}h - b \ln\left(\frac{T_o}{T_R}\right) - c(\bar{T}_R - T_o) &= F_{sun}he^{-\frac{\bar{Z}}{h}} \\
\Rightarrow \frac{\bar{Z}}{h} \underbrace{\frac{F_{geo} + \rho_{ice}vL(1 - \gamma_{glacier})}{F_{sun}}}_{\alpha} & \\
+ 1 - \underbrace{\frac{b \ln\left(\frac{T_o}{T_R}\right) + c(\bar{T}_R - T_o)}{F_{sun}h}}_{\beta} &= e^{-\frac{\bar{Z}}{h}} \\
\Rightarrow \frac{\bar{Z}}{h} \alpha + \beta &= e^{-\frac{\bar{Z}}{h}}
\end{aligned} \tag{49}$$

We introduce a new variable Y defined as :

$$\bar{Z} = \left(Y - \frac{\beta}{\alpha}\right)h \tag{50}$$

and use it to change variable in Eq. (49):

$$\begin{aligned}
\frac{\bar{Z}}{h} \alpha + \beta &= e^{-\frac{\bar{Z}}{h}} \\
\Rightarrow \frac{\left(Y - \frac{\beta}{\alpha}\right)h}{h} \alpha + \beta &= e^{-\frac{\left(Y - \frac{\beta}{\alpha}\right)h}{h}} \\
\Rightarrow \alpha Y &= e^{-Y} e^{\frac{\beta}{\alpha}} \\
\Rightarrow Y e^Y &= \frac{e^{\frac{\beta}{\alpha}}}{\alpha} \\
\Rightarrow \underbrace{W\left(Y e^Y\right)}_Y &= W\left(\frac{e^{\frac{\beta}{\alpha}}}{\alpha}\right)
\end{aligned} \tag{51}$$

Where W is the Lambert-W function, defined as:

$$Y = W(Ye^Y) \tag{52}$$

Finally, from Eq. (52) and Eq. (50) we derive the analytic solution for the ice thickness in Eq. (20):

$$\bar{Z} = h \left(W\left(\frac{e^{\frac{\beta}{\alpha}}}{\alpha}\right) - \frac{\beta}{\alpha} \right) \tag{53}$$

with α and β defined in Eq. (49). The Lambert-W function is available in many scientific programming languages and a uniform approximation from [Winitzki \(2003\)](#) with a relative error $<10^{-2}$ is repeated here for convenience:

$$\left\{ \begin{array}{l}
 W(x) = \left(2 \log(1 + B \sqrt{2ex + 2}) \right. \\
 \left. - \log(1 + C \log(1 + D \sqrt{2ex + 2})) + E \right) \\
 \times \frac{1}{1 + 1/(2 \log(1 + B \sqrt{2ex + 2}) + 2A)} \\
 \\
 e = 2.71828... \quad A = 2.344 \quad B = 0.8842 \\
 C = 0.9294 \quad D = 0.5106 \quad E = -1.213
 \end{array} \right. \quad (54)$$

Acknowledgements

The authors thank Michael D. Smith for his valuable assistance to update the correlated-k coefficients used in the NASA Ames radiative transfer code, the NASA Ames Mars Climate Modeling Center (MCMC) who provided support this project as well as the anonymous reviewer and Dr Edwin Kite for their careful reviews which greatly improved this paper.

References

References

- AASCE (1993). Design and construction of urban stormwater management systems. *American Society of Civil Engineers*, 77:91.
- Adams, E., Cosler, D., and Helfrich, K. (1990). Evaporation from heated water bodies: Predicting combined forces plus free convection. *Water Resources Research*, 26:425–435.
- Allison, M. and McEwen, M. (2000). A post-pathfinder evaluation of areocentric solar coordinates with improved timing recipes for Mars seasonal/diurnal climate studies. *Planetary and Space Science*, 48:215 – 235.
- Altheide, T., Chevier, V., Nicholson, C., and Denson, J. (2009). Experimental investigation of the stability and evaporation of sulfate and chloride brines on Mars. *Earth and Planetary Science letters*, 282:69–78.
- Andersen, D. T., McKay, C. P., and Lagun, V. (2015). Climate conditions at perennially-covered lake Untersee, east Antarctica. *JAMS*, 54:1393–1412.
- Andersen, D. T., Sumner, D. Y., Hawes, I., Webster-Brown, J., and McKay, C. P. (2011). Discovery of large conical stromatolites in lake Untersee, Antarctica. *Geobiology*, 9(3):280–293.
- Anderson, R., Bridges, J., Williams, A., Edgar, L., Ollila, A., Williams, J., Nachon, M., Mangold, N., Fisk, M., Schieber, J., Gupta, S., Dromart, G., Wiens, R., MouÛl'lic, S. L., Forni, O., Lanza, N., Mezzacappa, A., Sautter, V., Blaney, D., Clark, B., Clegg, S., Gasnault, O., Lasue, J., L'Al' veill'Al', R., Lewin, E., Lewis, K., Maurice, S., Newsom, H., Schwenzer, S., and Vaniman, D. (2015). ChemCam results from the shaler outcrop in Gale crater, Mars. *Icarus*, 249:2 – 21. Special Issue: First Year of MSL.
- Armitage, K. B. and House, H. B. (1962). A limnological reconnaissance in the area of Mcmurdo sound, Antarctica. *Limnology and Oceanography*, 7(1):36–41.
- Bahcall, J. N., Pinsonneault, M. H., and Basu, S. (2001). Solar models: Current epoch and time dependences, neutrinos, and helioseismological properties. *The Astrophysical Journal*, 555(2):990–1012.
- Barabash, S., Fedorov, A., Lundin, R., and Sauvaud, J.-A. (2007). Martian atmospheric erosion rates. *Science*, 315, Issue 5811:501–503.
- Batalha, N. E., Kopparapu, R. K., Haqq-Misra, J., and Kasting, J. F. (2016). Climate cycling on early Mars caused by the carbonate-silicate cycle. *Earth and Planetary Science Letters*, 455:7–13.

- Berger, A. and Loutre, M. (1994). Precession, eccentricity, obliquity, insolation and paleoclimates. *Long-Term Climatic Variations, Springer, Berlin, Heidelberg*, 22:107–151.
- Bevington, J., McKay, C., Davila, A., Hawes, I., Tanabe, Y., and Andersen, D. (2018). The thermal structure of the anoxic trough in lake Untersee, Antarctica. *Antarctic Science*, pages 1–12.
- Bohren, C. F. (1983). Colors of snow, frozen waterfalls, and icebergs. *J. Opt. Soc. Am.*, 73(12):1646–1652.
- Bristow, T. F., Haberle, R. M., Blake, D. F., Des Marais, D. J., Eigenbrode, J. L., Fairén, A. G., Grotzinger, J. P., Stack, K. M., Mischna, M. A., Rampe, E. B., Siebach, K. L., Sutter, B., Vaniman, D. T., and Vasavada, A. R. (2017). Low Hesperian PCO₂ constrained from in situ mineralogical analysis at Gale crater, Mars. *PNAS*, 114 no. 9:2166–2170.
- Carr, M. H. and Head, J. W. (2010). Geologic history of Mars. *Earth and Planetary Science Letters*, 294(3):185 – 203.
- Chittenden, J., Chevrier, V., Roe, L., Bryson, K., Pilgrim, R., and Sears, D. (2008). Experimental study of the effects of wind on the stability of water ice on Mars. *Icarus*, 196:477–487.
- Christensen, P. R., Bandfield, J. L., Hamilton, V. E., Ruff, S. W., Kieffer, H. H., Titus, T. N., Malin, M. C., Morris, R. V., Lane, M. D., Clark, R. L., Jakosky, B. M., Mellon, M. T., Pearl, J. C., Conrath, B. J., Smith, M. D., Clancy, R. T., Kuzmin, R. O., Roush, T., Mehall, G. L., Gorelick, N., Bender, K., Murray, K., Dason, S., Greene, E., Silverman, S., and Greenfield, M. (2001). Mars Global Surveyor Thermal Emission Spectrometer experiment: Investigation description and surface science results. *Journal of Geophysical Research: Planets*, 106(E10):23823–23871.
- Clifford, S. M. and Costard, F. (2017). Geomorphic evidence for a late hesperian northern ocean and its implications for the noachian. *Fourth Conference on Early Mars, Flagstaff, Arizona*, 2014.
- Clifford, S. M. and Parker, T. J. (2001). The evolution of the martian hydrosphere: implications for the fate of a primordial ocean and the current state of the northern plains. *Icarus*, 154(1):40 – 79.
- Craig, H., H., S., and Langway, C. C. (1993). Nonequilibrium air clathrate hydrates in antarctic ice : a paleopiezometer for polar ice caps. *Proceedings of the National Academy of Sciences of the United States of America*, 90(23):11416–11418. eng.
- Deit, L. L., Hauber, E., Fueten, F., Pondrelli, M., Rossi, A. P., and Jaumann, R. (2013). Sequence of infilling events in Gale crater, Mars: Results from morphology, stratigraphy, and mineralogy. *Journal of Geophysical Research: Planets*, 118(12):2439–2473.
- Doran, P., Wharton, R., Lyons, W., and Paleolimnol, J. (1994). Paleolimnology of the McMurdo Dry valleys, Antarctica. *Journal of Paleolimnology*, 10(2).
- Dundas, C. M. and Byrne, S. (2010). Modeling sublimation of ice exposed by new impacts in the martian mid-latitudes. *Icarus*, 206:716–728.
- Edgar, L. A., Gupta, S., Rubin, D. M., Lewis, K. W., Kocurek, G. A., Anderson, R. B., Bell III, J. F., Dromart, G., Edgett, K. S., Grotzinger, J. P., Hardgrove, C., Kah, L. C., Leveille, R., Malin, M. C., Mangold, N., Milliken, R. E., Minitti, M., Palucis, M., Rice, M., Rowland, S. K., Schieber, J., Stack, K. M., Sumner, D. Y., Wiens, R. C., Williams, R. M. E., and Williams, A. J. (2018). Shaler: in situ analysis of a fluvial sedimentary deposit on Mars. *Sedimentology*, 65(1):96–122.
- Edwards, C. and Ehlmann, B. (2015). Carbon sequestration on Mars. *Geology*, 43:863–866.
- Fairén, A. G., Stokes, C. R., Davies, N. S., Schulze-Makuch, D., Rodríguez, J. A. P., Davila, A. F., Uceda, E. R., Dohm, J. M., Baker, V. R., Clifford, S. M., McKay, C. P., and Squyres, S. W. (2014). A cold hydrological system in Gale crater, Mars. *Planetary and Space Science*, 93-94:101–118.
- Fanale, F. P., Salvail, J. R., Banerdt, W. B., and Saunders, R. S. (1982). Mars: The regolith-atmosphere-cap system and climate change. *Icarus*, 50(2):381 – 407.

- Faucher, B., Lacelle, D., Fisher, D., Andersen, D., and McKay, C. (2019). Energy and water mass balance of lake Untersee and its perennial ice cover, east Antarctica. *Antarctic Science*, 66:1–15.
- Forget, F., Byrne, S., Head, J. W., Mischna, M. A., and SchÄurghofer, N. (2017). Recent climate variations. *The Atmosphere and Climate of Mars*, Cambridge University Press, pages 497–526.
- Forget, F., Wordsworth, R., Millour, E., Kerber, L., J.Leconte, Marcq, E., and Haberle, R. (2013). Modelling of the early martian climate under a denser CO₂ atmosphere: temperatures and CO₂ ice clouds. *Icarus*, 222:81–99.
- Golombek, M. P., Grant, J. A., Crumpler, L. S., Greeley, R., Arvidson, R. E., Bell, J. F., Weitz, C. M., Sullivan, R., Christensen, P. R., Soderblom, L. A., and Squyres, S. W. (2006). Erosion rates at the Mars Exploration Rover landing sites and long-term climate change on Mars. *Journal of Geophysical Research: Planets*, 111(E12):n/a–n/a. E12S10.
- Gough, D. O. (1981). Solar interior structure and luminosity variations. *Solar Physics*, 74(1):21–34.
- Grant, J. A., Wilson, S. A., Mangold, N., Calef, F., and Grotzinger, J. P. (2014). The timing of alluvial activity in Gale crater, Mars. *Geophysical Research Letters*, 41(4):1142–1149. 2013GL058909.
- Grott, M., Helbert, J., and Nadalini, R. (2007). Thermal structure of martian soil and the measurability of the planetary heat flow. *Journal of Geophysical Research: Planets*, 112(E9):n/a–n/a. E09004.
- Grotzinger, J. P., Gupta, S., Malin, M. C., Rubin, D. M., Schieber, J., Siebach, K., Sumner, D. Y., Stack, K. M., Vasavada, A. R., Arvidson, R. E., Calef, F., Edgar, L., Fischer, W. F., Grant, J. A., Griffes, J., Kah, L. C., Lamb, M. P., Lewis, K. W., Mangold, N., Minitti, M. E., Palucis, M., Rice, M., Williams, R. M. E., Yingst, R. A., Blake, D., Blaney, D., Conrad, P., Crisp, J., Dietrich, W. E., Dromart, G., Edgett, K. S., Ewing, R. C., Gellert, R., Hurowitz, J. A., Kocurek, G., Mahaffy, P., McBride, M. J., McLennan, S. M., Mischna, M., Ming, D., Milliken, R., Newsom, H., Oehler, D., Parker, T. J., Vaniman, D., Wiens, R. C., and Wilson, S. A. (2015). Deposition, exhumation, and paleoclimate of an ancient lake deposit, Gale crater, Mars. *Science*, 350(6257).
- Grotzinger, J. P., Sumner, D. Y., Kah, L. C., Stack, K., Gupta, S., Edgar, L., Rubin, D., Lewis, K., Schieber, J., Mangold, N., Milliken, R., Conrad, P. G., DesMarais, D., Farmer, J., Siebach, K., Calef, F., Hurowitz, J., McLennan, S. M., Ming, D., Vaniman, D., Crisp, J., Vasavada, A., Edgett, K. S., Malin, M., Blake, D., Gellert, R., Mahaffy, P., Wiens, R. C., Maurice, S., Grant, J. A., Wilson, S., Anderson, R. C., Beegle, L., Arvidson, R., Hallet, B., Sletten, R. S., Rice, M., Bell, J., Griffes, J., Ehlmann, B., Anderson, R. B., Bristow, T. F., Dietrich, W. E., Dromart, G., Eigenbrode, J., Fraeman, A., Hardgrove, C., Herkenhoff, K., Jandura, L., Kocurek, G., Lee, S., Leshin, L. A., Leveille, R., Limonadi, D., Maki, J., McCloskey, S., Meyer, M., Minitti, M., Newsom, H., Oehler, D., Okon, A., Palucis, M., Parker, T., Rowland, S., Schmidt, M., Squyres, S., Steele, A., Stolper, E., Summons, R., Treiman, A., Williams, R., Yingst, A., and Team, M. S. (2014). A habitable fluvio-lacustrine environment at Yellowknife bay, Gale crater, Mars. *Science*, 343(6169).
- Haberle, R. (2013). Estimating the power of Mars’ greenhouse effect. *Icarus*, 223:619–620.
- Haberle, R., Catling, D., Carr, M., and Zahnle, K. (2017). The early Mars climate system. *The atmosphere and climate of Mars*, Cambridge University Press, pages 526–568.
- Haberle, R. M., Kahre, M. A., Hollingsworth, J. L., Montmessin, F., Wilson, R. J., Urata, R. A., Brecht, A. S., Wolff, M. J., Kling, A. M., and Schaeffer, J. R. (2019). Documentation of the NASA/Ames Legacy Mars Global Climate Model: Simulations of the present seasonal water cycle. *Icarus*, 333:130 – 164.
- Haberle, R. M., McKay, C. P., Schaeffer, J., Cabrol, N. A., Grin, E. A., Zent, A. P., and Quinn, R. (2001). On the possibility of liquid water on present-day Mars. *Journal of Geophysical Research*, 106:23,317–23,326.
- Havelly, I. and Head, J. W. I. (2014). Episodic warming of early Mars by punctuated volcanism. *Nature Geoscience*, 7:865–868.
- Hawes, I., Sumner, D. Y., Andersen, D. T., Jungblut, A. D., and Mackey, T. J. (2013). Timescales of growth response of microbial mats to environmental change in an ice-covered antarctic lake. *Biology*, 2(1):151–176.
- Head, J. W. and Marchant, D. R. (2014). The climate history of early Mars: insights from the Antarctic Mcmurdo Dry valleys hydrologic system. *Antarctic Science*, 26(6):774–800.

- Hecht, M. H. (2002). Metastability of liquid water in Mars. *Icarus*, 156:373–386.
- Hoffert, M., Callegari, A., Hsieh, C., and Ziegler, W. (1981). Liquid water on Mars: an energy balance climate model for CO₂/H₂O atmospheres. *Icarus*, 47:112–129.
- Hottel, H. (1976). Simple model for estimating the transmittance of direct solar radiation through clear atmospheres. *Sol. Energy; (United States)*, 18:2.
- Hu, R., Kass, D. M., Ehlmann, B. L., and Yung, Y. L. (2015). Tracing the fate of carbon and the atmospheric evolution of Mars. *Nature Communications*, 6.
- Hurowitz, J. A., Grotzinger, J. P., Fischer, W. W., McLennan, S. M., Milliken, R. E., Stein, N., Vasavada, A. R., Blake, D. F., Dehouck, E., Eigenbrode, J. L., Fairén, A. G., Frydenvang, J., Gellert, R., Grant, J. A., Gupta, S., Herkenhoff, K. E., Ming, D. W., Rampe, E. B., Schmidt, M. E., Siebach, K. L., Stack-Morgan, K., Sumner, D. Y., and Wiens, R. C. (2017). Redox stratification of an ancient lake in Gale crater, Mars. *Science*, 356(6341).
- Ingersoll, A. P. (1971). MARS: Occurrence of liquid water. *Sagan et al. eds, Planetary Atmospheres*, pages 247–250.
- Irwin, R. P., Maxwell, T. A., Howard, A. D., Craddock, R. A., and Leverington, D. W. (2002). A large paleolake basin at the head of ma'adim vallis, Mars. *Science*, 296(5576):2209–2212.
- Jakosky, B. M., Slipski, M., Benna, M., Mahaffy, P., Elrod, M., Yelle, R., Stone, S., and Alsaeed, N. (2017). Mars atmospheric history derived from upper-atmosphere measurements of 38ar/36ar. *Science*, 355(6332):1408–1410.
- Kahre, M. A., Vines, S. K., Haberle, R. M., and Hollingsworth, J. L. (2013). The early martian atmosphere: Investigating the role of the dust cycle in the possible maintenance of two stable climate states. *Journal of Geophysical Research: Planets*, 118:1388–1396.
- Kasting, J. F. (1991). CO₂ condensation and the climate of early Mars. *Icarus*, 94:1–13.
- Kite, E., Gao, P., Goldblatt, C., A. Mischna, M., Mayer, D., and Yung, Y. (2017). Methane bursts as a trigger for intermittent lake-forming climates on post-Noachian Mars. *Nature Geoscience*, 10.
- Kite, E. S., Halevy, I., Kahre, M. A., Wolff, M. J., and Manga, M. (2013). Seasonal melting and the formation of sedimentary rocks on Mars, with predictions for the Gale crater mound. *Icarus*, 223(1):181 – 210.
- Kite, E. S., Williams, J.-P., Lucas, A., and Aharonson, O. (2014). Low palaeopressure of the martian atmosphere estimated from the size distribution of ancient craters. *Nature Geoscience*, 7:335–339.
- Laskar, J., Levrard, B., and Mustard, J. F. (2002). Orbital forcing of the martian polar layered deposits. *Nature*, 419:375–377.
- Leblanc, F. and Johnson, R. (2002). Role of molecular species in pickup ion sputtering of the martian atmosphere. *JGR*, 107, Issue E2:51–56.
- Levine, J. S., Kraemer, D. R., and Kuhn, W. R. (1977). Solar radiation incident on Mars and the outer planets: Latitudinal, seasonal, and atmospheric effects. *Icarus*, 31(1):136 – 145.
- Levitan, M. A., Girin, Y. P., Luksha, V. L., Kubrakova, I. V., Roshchina, I. A., Sattler, B., Tyutyunnik, O. A., and Chudetskii, M. Y. (2011). Modern sedimentation system of lake Untersee, east Antarctica. *Geochemistry International*, 49(5):459–481.
- Liu, B. and Jordan, R. (1960). The interrelationship and characteristic distribution of direct, diffuse and total solar radiation. *Solar Energy*, 4(3):1 – 19.
- M. Jepsen, S., Adams, E., and C. Priscu, J. (2010). Sediment melt-migration dynamics in perennial antarctic lake ice. *Arctic Antarctic and Alpine Research*, 42:57–66.
- Mackey, T. J., Sumner, D. Y., Hawes, I., Jungblut, A. D., and Andersen, D. T. (2015). Growth of modern branched columnar stromatolites in lake joyce, Antarctica. *Geobiology*, 13(4):373–390.

- Mansfield, M., Kite, E. S., and Mischna, M. A. (2018). Effect of Mars atmospheric loss on snow melt potential in a 3.5 gyr Mars climate evolution model. *Journal of Geophysical Research: Planets*, 123(4):794–806.
- Marchant, D. R. and Head, J. W. I. (2007). Antarctic Dry valleys: Microclimate zonation, variable geomorphic processes, and implications for assessing climate change on Mars. *Icarus*, 192(1):187 – 222.
- Martínez, G. M., Newman, C. N., De Vicente-Retortillo, A., Fischer, E., Renno, N. O., Richardson, M. I., Fairén, A. G., Genzer, M., Guzewich, S. D., Haberle, R. M., Harri, A.-M., Kempainen, O., Lemmon, M. T., Smith, M. D., de la Torre-Juárez, M., and Vasavada, A. R. (2017). The modern near-surface martian climate: A review of in-situ meteorological data from viking to curiosity. *Space Science Reviews*, 212(1):295–338.
- Martínez-Torres, F. J., Zorzano, M.-P., Valentín-Serrano, P., Harri, A.-M., Genzer, M., Kempainen, O., Rivera-Valentín, E. G., Hardgrove, C., Renno, N., Chevrier, V. F., Mischna, M., Navarro-González, R., Martínez-Frías, J., Conrad, P., McConnochie, T., Cockell, C., Berger, G., R. Vasavada, A., Sumner, D., and Vaniman, D. (2015). Transient liquid water and water activity at Gale crater on Mars. *Nature Geoscience*, 8:357–361.
- Matsubara, Y., Howard, A. D., and Drummond, S. A. (2011). Hydrology of early Mars: Lake basins. *Journal of Geophysical Research: Planets*, 116(E4).
- McKay, C., Clow, G., Wharton Jr., R., and Squyres, S. W. (1985). Thickness of ice on perennially frozen lakes. *nature*, 313:561–562.
- McKay, C. P. (2004). *Thin Ice on the Snowball Earth*, pages 193–198. American Geophysical Union (AGU).
- McKay, C. P., Clow, G. D., Andersen, D. T., and Wharton, R. A. (1994). Light transmission and reflection in perennially ice-covered lake hoare, Antarctica. *Journal of Geophysical Research: Oceans*, 99(C10):20427–20444.
- McKay, C. P. and Davis, W. L. (1991). Duration of liquid water habitats on early Mars. *Icarus*, 90(2):214 – 221.
- Ming, D. W., Archer, P. D., Glavin, D. P., Eigenbrode, J. L., Franz, H. B., Sutter, B., Brunner, A. E., Stern, J. C., Freissinet, C., McAdam, A. C., Mahaffy, P. R., Cabane, M., Coll, P., Campbell, J. L., Atreya, S. K., Niles, P. B., Bell, J. F., Bish, D. L., Brinckerhoff, W. B., Buch, A., Conrad, P. G., Des Marais, D. J., Ehlmann, B. L., Fairén, A. G., Farley, K., Flesch, G. J., Francois, P., Gellert, R., Grant, J. A., Grotzinger, J. P., Gupta, S., Herkenhoff, K. E., Hurowitz, J. A., Leshin, L. A., Lewis, K. W., McLennan, S. M., Miller, K. E., Moersch, J., Morris, R. V., Navarro-González, R., Pavlov, A. A., Perrett, G. M., Pradler, I., Squyres, S. W., Summons, R. E., Steele, A., Stolper, E. M., Sumner, D. Y., Szopa, C., Teinturier, S., Trainer, M. G., Treiman, A. H., Vaniman, D. T., Vasavada, A. R., Webster, C. R., Wray, J. J., and Yingst, R. A. (2014). Volatile and organic compositions of sedimentary rocks in Yellowknife bay, Gale crater, Mars. *Science*, 343(6169).
- Montgomery, W., Bromiley, G. D., and Sephton, M. A. (2016). The nature of organic records in impact excavated rocks on Mars. *Scientific Reports*, 6(30947).
- Mühlmann, D. and Thomsen, K. (2011). Properties of cryobrine on Mars. *Icarus*, 212(1):123 – 130.
- Nadeau, A. and McGehee, R. (2017). A simple formula for a planet’s mean annual insolation by latitude. *Icarus*, 291:46 – 50.
- NOAA (2015). Climate normals. *Comparative Climatic Data*.
- North, G. R. (1975a). Analytical Solution to a Simple Climate Model with Diffusive Heat Transport. *Journal of Atmospheric Sciences*, 32:1301–1307.
- North, G. R. (1975b). Theory of Energy-Balance Climate Model. *Journal of Atmospheric Sciences*, 32:2033–2043.
- Obryk, M., Doran, P. T., Hicks, J. A., McKay, C. P., and Priscu, J. C. (2016). Modeling the thickness of perennial ice covers on stratified lakes of the Taylor Valley, Antarctica. *Journal of Glaciology*, 62:825–834.
- Oehler, D. Z., Mangold, N., Hallet, B., Fairén, A. G., Deit, L. L., Williams, A. J., Sletten, R. S., and Martínez-Frías, J. (2016). Origin and significance of decameter-scale polygons in the lower Peace vallis fan of Gale crater, Mars. *Icarus*, 277:56–72.

- Palucis, M. C., Dietrich, W. E., Hayes, A. G., Williams, R. M. E., Gupta, S., Mangold, N., Newsom, H., Hardgrove, C., Calef, F., and Sumner, D. Y. (2014). The origin and evolution of the Peace Vallis fan system that drains to the curiosity landing area, Gale crater, Mars. *Journal of Geophysical Research: Planets*, 119(4):705–728. 2013JE004583.
- Pavlov, A. A., Vasilyev, G., Ostryakov, V. M., Pavlov, A. K., and Mahaffy, P. (2012). Degradation of the organic molecules in the shallow subsurface of Mars due to irradiation by cosmic rays. *Geophysical Research Letters*, 39(13). L13202.
- Postawko, S. E. and Kuhn, W. R. (1986). Effect of the greenhouse gases (CO₂, H₂O, SO₂) on martian paleoclimate. *Journal of Geophysical Research: Solid Earth*, 91(B4):431–438.
- Priscu, J. C., Wolf, C. F., Takacs, C. D., Fritsen, C. H., Laybourn-Parry, J., Roberts, E. C., Sattler, B., and Lyons, W. B. (1999). Carbon transformations in a perennially ice-covered antarctic lake. *BioScience*, 49(12):997–1008.
- Rafkin, S. C. R., Hollingsworth, J. L., Mischna, M. A., Newman, C. E., and Richardson, M. I. (2013). Mars: Atmosphere and climate overview. *Comparative Climatology of Terrestrial Planets, Univ. of Arizona, Tucson*, pages 55–88.
- Ramirez, R. M., Kopparapu, R., Zuger, M. E., Robinson, T. D., Freedman, R., and Kasting, J. F. (2014). Warming early Mars with CO₂ and H₂. *Nature Geoscience*, 7:59–63.
- Read, P. L., Lewis, S. R., and Mulholland, D. P. (2015). The physics of martian weather and climate: a review. *Reports on Progress in Physics*, 78(12):125901.
- Richardson, C. and Holmlund, P. (1996). Glacial cirque formation in northern Scandinavia. *Annals of Glaciology*, 22:102–106.
- Rivera-Hernandez, F., Sumner, D. Y., Mackey, T. J., Hawes, I., and Andersen, D. T. (2019). In a picl: The sedimentary deposits and facies of perennially ice-covered lakes. *Sedimentology*, 66(3):917–939.
- Robinson, T. D. and Catling, D. C. (2012). An analytic radiative-convective model for planetary atmospheres. *The Astrophysical Journal*, 757(1):104.
- Savijarvi, H. (1999). A model study of the atmospheric boundary layer in the Mars Pathfinder lander conditions. *Quarterly Journal of the Royal Meteorological Society*, 125(554):483–493.
- Schubert, G. and Mitchell, J. (2013). Planetary atmospheres as heat engines. *Comparative climatology of terrestrial planets*, pages 181–191.
- Segura, T. L., McKay, C. P., and Toon, O. B. (2012). An impact-induced, stable, runaway climate on Mars. *Icarus*, 220:144–148.
- Shaw, J. and Healy, T. (1980). Morphology of the Onyx river system, Mcmurdo sound region, Antarctica. *New Zealand journal of geology and geophysics*, 23(2):223–238.
- Simmons, G. M. J., Wharton, R. A. J., McKay, C. P., Nedell, S., and Clow, G. (1987). Sand/ice interactions and sediment deposition in perennially-ice covered antarctic lakes. *Antarctic journal*, 21:217–220.
- Smith, M. D., Bougher, S. W., Encrenaz, T., Forget, F., and Kleinböhl, A. (2017). Thermal structure and composition. *The Atmosphere and Climate of Mars, Cambridge University Press*, pages 42–75.
- Sokratova, I. N. (2011). Hydrological investigations in the antarctic oases. *Russian Meteorology and Hydrology*, 36:207–215.
- Squyres, S., Andersen, D., Nedell, S., and Wharton, R. A. J. (1991). Lake hoare, Antarctica: sedimentation through a thick perennial ice cover. *Sedimentology*, 38(2):363–379.
- Steakley, K., Murphy, J., Kahre, M., Haberle, R., and Kling, A. (2019). Testing the impact heating hypothesis for early Mars with a 3-D global climate model. *Icarus*, 330:169 – 188.

- Steel, H. C. B., McKay, C. P., and Andersen, D. T. (2015). Modeling circulation and seasonal fluctuations in perennially ice-covered and ice-walled lake Untersee, Antarctica. *Limnology and Oceanography*, 60(4):1139–1155.
- Stoker, C., Gooding, J., Roush, T., Banin, A., Burt, D., Clark, B., Flynn, G., and Gwynne, O. (1993). The physical and chemical properties and resource potential of martian surface soils. *Resources of near-Earth space*.
- Sumner, D. Y., Jungblut, A. D., Hawes, I., Andersen, D. T., Mackey, T. J., and Wall, K. (2016). Growth of elaborate microbial pinnacles in lake vanda, Antarctica. *Geobiology*, 14(6):556–574.
- Thomson, B., Bridges, N., Milliken, R., Baldrige, A., Hook, S., Crowley, J., Marion, G., de Souza Filho, C., Brown, A., and Weitz, C. (2011). Constraints on the origin and evolution of the layered mound in Gale crater, Mars using Mars Reconnaissance Orbiter data. *Icarus*, 214(2):413 – 432.
- Tosca, N. J., Ahmed, I. A. M., Tutolo, B. M., Ashpitel, A., and Hurowitz, J. A. (2018). Magnetite authigenesis and the warming of early Mars. *Nature Geoscience*, 11:635–639.
- Townsend, A., Pikuta, E., Guisler, M., Stahl, S., and B. Hoover, R. (2009). Anaerobic psychrophiles from lake zub and lake Untersee, Antarctica. *SPIE, San Diego, CA*, 7441.
- Von Paris, P., Petau, A., Grenfell, J., Hauber, E., Breuer, D., and Jaumann, R. (2015). Estimating precipitation on early Mars using a radiative-convective model of the atmosphere and comparison with inferred runoff from geomorphology. *Planetary and Space Science*, 105:133–147.
- Wand, U., Schwarz, G., Brüggemann, E., and Bräuer, K. (1997). Evidence for physical and chemical stratification in lake Untersee (central dronning maud land, east Antarctica. *Antarctic Science*, 9:43–45.
- Wang, J. and Bras, R. L. (2001). Effect of temperature on surface energy balance. *Water Resources Research*, 37(12):3383–3386.
- Williams, D. M. and Kasting, J. F. (1997). Habitable planets with high obliquities. *Icarus*, 129(1):254 – 267.
- Williams, K., Toon, O., Heldmann, J., McKay, C., and Mellon, M. (2008). Stability of mid-latitude snowpack on Mars. *Icarus*, 196:565–577.
- Williams, R., Grotzinger, J., Dietrich, W., Gupta, S., Sumner, D., Wiens, R., Mangold, N., Malin, M., Edgett, K., Maurice, S., Forni, O., Gasnault, O., Ollila, A., Newsom, H., Dromart, G., Palucis, M., Yingst, R., Anderson, R., Herkenhoff, K., Le Mouelic, S., Goetz, W., Madsen, M., Koefoed, A., Jensen, J., Bridges, J., Schwenzer, S., Lewis, K., Stack, K., Rubin, D., Kah, L., Bell, J., Farmer, J., Sullivan, R., Van Beek, T., Blaney, D., Pariser, O., and Deen, R. (2013). Martian fluvial conglomerates at Gale crater. *Science*, 340(6136):1068–1072.
- Winitzki, S. (2003). *Uniform Approximations for Transcendental Functions*, volume 2667, chapter 2667. Kumar V., et al. (eds) Computational Science and Its Applications, Springer.
- Wordsworth, R., Forget, F., and Eymet, V. (2010). Infrared collision-induced and far-line absorption in dense CO₂ atmospheres. *Icarus*, 210(2):992 – 997.
- Wordsworth, R., Forget, F., Millour, E., Head, J., Madeleine, J.-B., and Charnay, B. (2013). Global modelling of the early martian climate under a denser CO₂ atmosphere: Water cycle and ice evolution. *Icarus*, 222:1–19.
- Wordsworth, R., Kalugina, Y., Lokshantov, S., Vigasin, A., Ehlmann, B., Head, J., Sanders, C., and Wang, H. (2017). Transient reducing greenhouse warming on early Mars. *Geophysical Research Letters*, 44(2):665–671. 2016GL071766.
- Wordsworth, R. D. (2016). The climate of early Mars. *Annual Review of Earth and Planetary Science*, 44:1–31.
- Zent, A., Hudson, T., Hecht, M., Cobos, D., and Wood, S. (2009). Mars regolith thermal and electrical properties: Initial results of the phoenix thermal and electrical conductivity probe (tecp). *40th Lunar and Planetary Science Conference*.